

The Pennsylvania State University
The Graduate School
College of Earth and Mineral Sciences

PREDICTABILITY AND DYNAMICS OF THE 9-10 JUN 2003 SQUALL LINE
AND BOW ECHO EVENT DURING BAMEX

A Thesis in
Meteorology
by
Christopher Melhauser

© 2010 Christopher Melhauser

Submitted in Partial Fulfillment
of the Requirements
for the Degree of

Master of Science

May 2010

The thesis of Christopher Melhauser was reviewed and approved* by the following:

Fuqing Zhang
Professor of Meteorology
Thesis Advisor

Yvette Richardson
Associate Professor of Meteorology

Paul Markowski
Associate Professor of Meteorology

Johannes Verlinde
Associate Professor of Meteorology
Associate Head, Graduate Program in Meteorology

*Signatures are on file in the Graduate School.

Abstract

An ensemble of cloud-resolving Weather Research and Forecasting Model (WRF) forecasts initialized with perturbations from an ensemble Kalman filter (EnKF) analysis is used to explore the predictability of a bow echo event during the Bow Echo and MCV Experiment (BAMEX) on 9-10 June 2003. The success of multiple WRF deterministic forecasts during the BAMEX campaign suggested that deterministic numerical weather prediction of convective-scale processes had come to fruition. Large variability in evolution and mode of convection and the environment of ensemble members prove the contrary, highlighting the limit of practical predictability given realistic initial condition uncertainties provided by the EnKF analysis.

Even though most members forecast severe convective weather over a broad area, some of the members produce bow echoes very similar to that observed while others perform poorly, either producing the wrong convective mode or wrong intensity. Given strong spatial and temporal variability in the environment, it is found that commonly used severe storm predictors based on single soundings (e.g., CAPE, CIN, low-level shear) have very limited capability in forecasting this bow echo event. Nevertheless, averaging of 10 good members versus 10 poor members provides a clear difference in storm evolution, with environments of good members having stronger CAPE and shear along with an upper-level shortwave and the development of a squall line, while poor members having weaker CAPE and shear, along with a weaker upper-level shortwave forming back-building MCSs.

Two distinct storm modes within the ensemble indicate a bifurcation point between two regimes that is associated with upscale error growth due to moist convection. To further explore the bifurcation and this event's intrinsic predictability, a perfect model assumption is made in conjunction with a simulated reduction in initial condition spread in temperature, meridional and zonal winds, mixing ratio, and pressure to locate the divergence point between forecasts. In essence, the ensemble forecast and additional sensitivity experiments demonstrated that: (1) this storm's predictability has a practical limit given realistic initial condition spread and its predictability can be improved with more accurate initial conditions; (2) if the storm's initial conditions are near bifurcation points, there may be an intrinsic limit. The limit of both practical and intrinsic predictability highlights the demands of probabilistic and ensemble forecasts for cloud-resolving severe weather prediction.

Table of Contents

List of Figures	vi
Acknowledgments	ix
Chapter 1	
Introduction	1
1.1 Literature Review	1
1.1.1 Dynamics and environment of bow echo formation	2
1.1.2 BAMEX	7
1.1.3 Predictability	8
1.2 Study Objective	10
Chapter 2	
Case Overview	12
2.1 Synoptic Environment	12
2.2 Mesoscale Evolution	13
Chapter 3	
Experimental Design	15
3.1 Model Description	15
3.2 Ensemble Initialization	17
Chapter 4	
Ensemble Variability, Error Growth, and Practical Predictability	19
4.1 Ensemble Variability	19
4.2 Ensemble Member Cross-Section and Viability	28
4.3 Ensemble Error Growth	30
Chapter 5	
Ensemble Categorization and Basic Parameter Analysis	33
5.1 Categorization of ensemble and subjective ranking	33
5.2 Basic correlation and parameter analysis	35
Chapter 6	
Ensemble Spread and Predictability	41
6.1 Experimental setup	41
6.2 EFIG to EFIP variability	44

6.3	Moist processes error growth: local scale	45
6.4	Moist processes error growth: storm scale	50
6.5	Intrinsic predictability	52
Chapter 7		
	Concluding Remarks	57
7.1	Discussion and Summary	57
Bibliography		60

List of Figures

1.1	Bow echo evolution schematic. (Source: Fujita 1978 [1])	3
1.2	Bow echo cross-section evolution. (Source: Weisman 1993 [2])	4
1.3	Bow echo propagation associated with synoptic pattern (a) weak forcing and (b) strong dynamic forcing. (Source: Johns and Hirt 1987 [3])	6
1.4	Synoptic environmental patterns (a) “weak forcing” and (b) “strong dynamic forcing”. (Source: Johns 1993 [4])	6
2.1	FNL analysis valid 0000 UTC 10 Jun 2003 (a) 300-hPa PV (shaded every 0.5 PVU), height (every 50 m), and wind (full barb $5 \text{ m}\cdot\text{s}^{-1}$) (b) most unstable CAPE (shaded every $250 \text{ J}\cdot\text{kg}^{-1}$) and most unstable CIN (contoured every $20 \text{ J}\cdot\text{kg}^{-1}$) (c) 0-5km bulk shear (shaded every $3 \text{ m}\cdot\text{s}^{-1}$). The box in (a-c) denotes the high resolution 3.3 km domain.	12
2.2	Hydrological Prediction Center (HPC) surface analysis valid at 0000 UTC 10 Jun 2003.	13
2.3	Composite radar reflectivity (dBz) observed at (a) 1600 (b) 1800 (c) 2000 (d) 2200 UTC 09 Jun 2003; (e) 0000 (f) 0200 (g) 0400 (h) 0600 (i) 0800 UTC 10 Jun 2003.	14
3.1	Schematic of domains used in the study.	15
3.2	Root mean square error in temperature (K) and zonal wind ($\text{m}\cdot\text{s}^{-1}$) from the Meng and Zhang 2008[5] month long experiment between EnKf (red), WRF-3DVar (blue), and FNL-GFS (black). (Source: Meng and Zhang (2008) [5])	16
3.3	EnKF data assimilation cycle schematic.	17
4.1	Simulated radar reflectivity (dBZ), sea level pressure (hPa), and surface winds (full barb $5 \text{ m}\cdot\text{s}^{-1}$) for 20 ensembles members at 0600 UTC 10 Jun.	20
4.2	Simulated radar reflectivity (dBZ), sea level pressure (hPa), and surface winds (full barb $5 \text{ m}\cdot\text{s}^{-1}$) for initial conditions from ensemble mean and EnKF analysis (left), FNL and EnKF analysis (middle), and purely FNL analysis (right) at 0600 UTC 10 Jun.	21
4.3	Simulated radar reflectivity (dBZ), sea level pressure (hPa), and surface winds (full barb $\text{m}\cdot\text{s}^{-1}$) for (a) EN38 and (b) EN11 from 2100 UTC 9 Jun to 0600 UTC 10 Jun.	21
4.4	Pressure contours (525-, 530-, 535-hPa) on a 5.5 km constant height surface at 1200 UTC 9 Jun 2003 for (a) 10 good and 10 poor subjectively ranked ensemble members and (b) averaged deterministic ensemble members IG, IP, IM, I1, and I3.	23

4.5	Average environment for good and poor members at 2100 UTC 9 Jun indicating (a) 0.5km CAPE ($\text{J}\cdot\text{kg}^{-1}$); (b) 850-hPa winds ($\text{m}\cdot\text{s}^{-1}$), heights (m), and wind speed (shaded, $\text{m}\cdot\text{s}^{-1}$); (c) 0-3 km bulk shear ($\text{m}\cdot\text{s}^{-1}$).	24
4.6	Schematic of environmental setup for the good and poor members at the time of convective initiation, 2100 UTC 9 Jun 2003.	25
4.7	(a) good and (b) poor ensemble member average soundings for 2100 UTC 9 Jun at black star location in Figure 4.6.	26
4.8	Average environment for good and poor members at 0200 UTC 9 Jun indicating (a) simulated composite reflectivity (dBZ), surface winds ($\text{m}\cdot\text{s}^{-1}$), and sea level pressure (hPa); (b) 850-hPa winds ($\text{m}\cdot\text{s}^{-1}$), heights (m), and wind speed (shaded, $\text{m}\cdot\text{s}^{-1}$); (c) 300-hPa PV (shaded every 1 PVU) and heights (m).	27
4.9	Schematic of environment and storm evolution for the good and poor members at 0200 UTC 10 Jun 2003.	28
4.10	Bow analysis for ensemble member EN16 valid 0600 UTC 10 Jun 2003 (a) zoomed in bow region with maximum simulated reflectivity (shaded every 5 dBZ) and 3 km relative vorticity (contoured every $25\times 10^{-5} \text{ s}^{-1}$; dash = negative) (b) cross section with maximum simulated reflectivity (shaded every 5 dBZ) and cross section tangent storm relative winds (full barb $5 \text{ m}\cdot\text{s}^{-1}$). Line A-A' in (a) denotes cross section in (b).	29
4.11	Vertically averaged root mean difference total energy between all ensemble members and ensemble member average (shaded every $1 \text{ m}\cdot\text{s}^{-1}$) for (a) 1200 (b) 1800 (c) 2200 UTC 9 Jun 2003 (d) 0000 (e) 0200 (f) 0400 (g) 0600 (h) 0800 (i) 1000 UTC 10 Jun 2003.	31
4.12	Horizontally averaged root mean difference total energy between all ensemble members and ensemble member average shown every 3 h from 1200 UTC 09 Jun 2003 to 0900 UTC 10 Jun 2003.	32
5.1	Simulated ensemble average maximum reflectivity (shaded every 5 dBZ), sea level pressure (hPa), and horizontal wind (full barb $5 \text{ m}\cdot\text{s}^{-1}$) for the subjectively defined good and poor ensemble sets at 0600 UTC 10 Jun 2003.	33
5.2	(a) number of threshold (45 dBZ) grid points falling within the red box of (b) inside the 20 dBZ ensemble mean contour for each ensemble member at each time with averages of the subjective sets indicated by colored lines (b) initial and final grid boxes used in DO4 with ensemble average maximum reflectivity (shaded every 5 dBZ), sea level pressure (hPa), and horizontal wind (full barb $\text{m}\cdot\text{s}^{-1}$) used for average correlations and determining strength metric used in part (a).	34
5.3	Most unstable CAPE versus time for a small averaged point (yellow star designated on D04 map representing the point location - Lincoln, NE) for good (blue), fair (green), and poor (red) ensemble members.	36
5.4	(a) good and (b) poor ensemble member average soundings for 0600 UTC 10 Jun at Lincoln, NE (yellow star location in Figure 5.3).	37
5.5	(a) spatial average most unstable CAPE for each ensemble member versus time from 1200 UTC 9 Jun to 1200 UTC 10 Jun with averages indicated by the blue (good), green (fair), and red (poor) lines. (b) D04 with gray shaded region used to deduce temporal environmental averages.	38
5.6	(a) average potential vorticity in PVU for each ensemble member within the indicated box and mean contour in (b) versus time with blue (good), green (fair), and red (poor) lines indicating group averages.	40

6.1	Horizontal root mean difference total energy between EFIG, EFIP and ensemble member average shaded (every $1 \text{ m}\cdot\text{s}^{-1}$) for (a) 1200 (b) 1800 (c) 2200 UTC 9 Jun 2003; (d) 0000 (e) 0200 (f) 0400 (g) 0600 (h) 0800 (i) 1000 UTC 10 Jun 2003.	42
6.2	Vertical root mean difference total energy between EFIG, EFIP and total ensemble member average shown every 3 h from 1200 UTC 9 Jun to 0900 UTC 10 Jun 2003.	43
6.3	(a) power spectra of difference total energy between averaged initial perturbation deterministic forecasts at 1200 UTC 9 Jun; (b) diagram of initial perturbation and difference total energy magnitude for the averaged deterministic forecasts.	44
6.4	Simulated radar reflectivity (shaded every 5dBz), sea level pressure (hPa), and surface winds (full barb $5 \text{ m}\cdot\text{s}^{-1}$) for subjectively defined good and poor averaged initial perturbation deterministic forecasts at 0400 UTC Jun 10. Red line indicates bifurcation point. (a) EFIG (b) EFIA (c) EFI1 (d) EFIB (e) EFIM (f) EFIC (g) EFI3 (h) EFID (i) EFIP.	45
6.5	(a) CAPE (0.25 km parcel) shaded every $250 \text{ J}\cdot\text{kg}^{-1}$ (b) CIN (0.25 km parcel) shaded every $25 \text{ J}\cdot\text{kg}^{-1}$ and 0-3 km bulk shear shaded every $3 \text{ m}\cdot\text{s}^{-1}$ for members EFIM and EFIC at 0100 UTC 10 JUN.	46
6.6	Simulated radar reflectivity (shaded every 5 dBz), sea level pressure (hPa), and surface winds (full barb $5 \text{ m}\cdot\text{s}^{-1}$) for EFIM (top) and EFIC (bottom) from 0000 to 0300 UTC Jun 10.	47
6.7	Surface virtual potential temperature (shaded every 2 K) and 700-hPa vertical velocity (contoured, solid black contour every $1 \text{ m}\cdot\text{s}^{-1}$ and dashed black every $-0.25 \text{ m}\cdot\text{s}^{-1}$) for EFIM (top) and EFIC (bottom) from 0000 to 0300 UTC Jun 10.	48
6.8	Environmental soundings for (a) EFIM and (b) EFIC ahead of the dryline near points C and D at 0100 UTC 10 Jun.	49
6.9	(a) surface CAPE shaded every $250 \text{ J}\cdot\text{kg}^{-1}$ (b) surface CIN shaded every $25 \text{ J}\cdot\text{kg}^{-1}$ (c) surface divergence shaded every 1 s^{-1} and (d) 0-3 km bulk shear $\text{m}\cdot\text{s}^{-1}$ for EFIG (left) and EFIP (right) at 2200 UTC 9 Jun.	51
6.10	Moss unstable CAPE shaded every $250 \text{ J}\cdot\text{kg}^{-1}$, surface dewpoint temperature K (dark blue contour), 0.5 km horizontal winds (full barb is $5 \text{ m}\cdot\text{s}^{-1}$), and 30 dBz simulated reflectivity contoured in white for EFIG (left) and EFIP (right) for 2200 UTC 9 Jun; 0000, 0200 UTC 10 Jun.	52
6.11	Idealized ensemble spread schematic of reducing initial condition error. The top schematic is representative of 9-10 Jun 2003 storm when the observed truth lies predominantly in one flow regime. The bottom shematic highlights a different case when the observed truth lies somewhere close to a divergence point between regimes.	53
6.12	(a) The time evolution of domain-integrated difference total energy (DTE) between specified members from 2200 UTC 9 Jun to 1200 UTC 10 Jun; (b) power spectra of DTE between specified members at: thin lines 0000 UTC 10 Jun and thick lines 0900 UTC 10 Jun.	55

Acknowledgments

I am forever grateful and in debt to my family for their support, motivation, encouragement, and to never let me settle. I thank my mom, Paula, as I would not be who I am today without her wisdom and guidance. I would like to express my sincere gratitude to my advisor, Fuqing Zhang, and to my other committee members, Yvette Richardson and Paul Markowski, for their support, guidance, and advice. Also, Meng Zhang and Yonghui Weng for their computer guidance and modeling support. I would like to thank the Department of Meteorology for providing a teaching assistantship during my time at Penn State, allowing me to pursue unfunded research in an area of strong interest.

Chapter 1

Introduction

Uncertainties in numerical weather prediction of squall lines, bow echoes, and other mesoscale convective systems (MCSs) are important in severe weather and forecast accuracy. Numerical weather prediction of the convective scales is a focus area of research with many studies using advanced neural networks and statistical algorithms to provide improved severe weather predictability. It is well documented that convective cells forming in certain environmental conditions can organize into a linear squall line from supercells, with subsequent bow echo formation producing damaging straight line surface winds. This study examines one such instance during the Bow Echo and MCV Experiment (BAMEX) on 9-10 Jun 2003 in which two supercell storms organized into a squall line structure with multiple bowing segments producing damaging surface winds in eastern Nebraska and western Iowa. The predictability along with the dynamics of the bow echo are examined.

1.1 Literature Review

This study makes use of a few well-known severe weather parameters that help forecasters deduce possible convective initiation location, subsequent evolution, and storm intensity. Two of these parameters are the convective available potential energy and convective inhibition.

Convective available potential energy (CAPE) is defined as the integrated buoyancy of a parcel of air between the levels of free convection and neutral buoyancy. A larger value of CAPE indicates larger atmospheric instability and more energy to produce stronger updrafts. Different measures of CAPE exist, depending on assumptions regarding the parcel. These include surface-based CAPE (SBCAPE), which measures the CAPE for a parcel lifted from the surface, most unstable CAPE (MUCAPE), which uses the parcel with the largest instability within the lowest 300 hPa of the atmosphere, and mixed layer CAPE (MLCAPE), which uses a theoretical parcel having properties representative of the lowest 100 hPa of the atmosphere[6].

Convective inhibition (CIN) is defined as the energy required to lift a parcel to the level of free convection. Larger values of CIN indicate more energy is needed for a parcel (surface,

mixed, or most unstable) to reach the level of free convection and thus initiate convection. Large values of CIN are usually indicative of capping inversions or layers of relatively warm air in the mid-troposphere. These capping inversions are a common occurrence in the central plains as warmed mixed layer air is advected from the higher plains to the west. Moderate CIN can suppress convection until enough mixing from sensible heating in the afternoon or convergence along a surface boundary allow parcels to reach their LFC[6].

1.1.1 Dynamics and environment of bow echo formation

Bow echoes are a weather phenomena that are known for causing long swaths of strong damaging straight-line winds. Nolen (1959) first identified a linear system of convective cells with multiple embedded bowing features associated with strong surface winds calling it a linear echo wave pattern (LEWP). Nolen (1959) described the LEWP as “a configuration of radar echoes in which a line of echoes has been subjected to an acceleration along one portion and/or a deceleration along that portion of the line immediately adjacent, with a resulting sinusoidal mesoscale wave pattern in a line”[7]. During studies by Fujita in the 70’s and 80’s after Nolen (specifically a study published from Project NIMROD on downbursts and microbursts in 1979), a synergy between the LEWP and downbursts was constructed studying the resultant damaging straight line winds that generally followed precipitation having a bow shaped radar echo, which Fujita coined a “bow echo” [1]. Fujita came up with a common theory from various field observations of the development of these mesoscale structures. Beginning as a single convective cell, group of convective cells, or a part of a squall line, they develop strong surface winds near the central axis. Fujita hypothesized that the strong straight-line winds (downburst) were associated with a strong rear inflow from behind the bow. During the formation of the bowing phase, this midlevel rear inflow accelerates towards the front of the line along the central axis causing the bowing structure. When extremely strong winds form along the central axis, a strongly bow shaped line known as a “spearhead” echo is possible, as seen in Figure 1.1. During the bow echo phase “bookend vortices”[2], or a pair of mesoscale vortices at the ends of convective line segments situated 2 to 4 km above the surface, develop with generally cyclonic rotation on the north and anticyclonic rotation on the south end of the line. A “comma” echo subsequently forms as the strong cyclonic vorticity on the northern end of the line dominates due to the Earth’s rotation.

Observational studies have shown that a relatively strong cold pool allows initial growth of the bow echo, along with medium to strong low level environmental shear and large amounts of CAPE ($\text{CAPE} > 2000 \text{ J}\cdot\text{kg}^{-1}$, although $500 \text{ J}\cdot\text{kg}^{-1}$ could suffice in a cold season, strongly forced case)[2]. A simple cross-section schematic of a rear inflow jet evolution is shown in Figure 1.2 with the environment characterized by strong shear ($> 20 \text{ m}\cdot\text{s}^{-1}$ in lowest 2.5 km) and large amounts of CAPE ($> 2000 \text{ J}\cdot\text{kg}^{-1}$). The evolution of this bow echo shows the creation of the rear inflow jet (RIJ) from the balance of the environmental shear and buoyancy fields as described below.

To develop the RIJ, the balance between the horizontal buoyancy gradients and the environ-

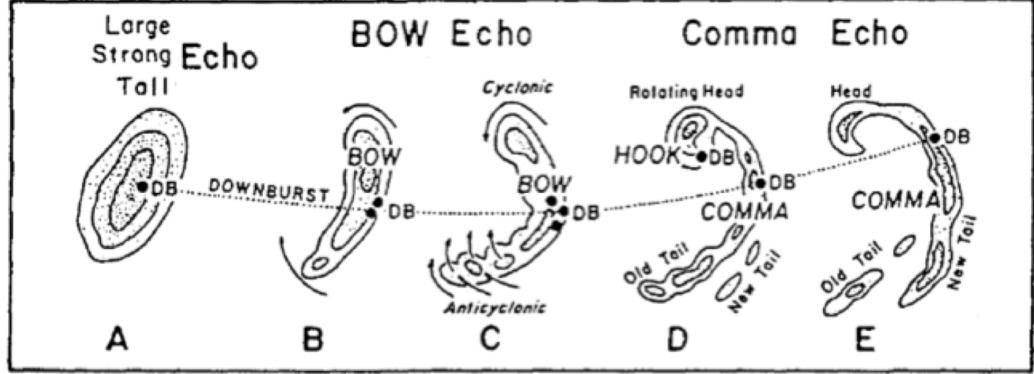


Figure 1.1. Bow echo evolution schematic. (Source: Fujita 1978 [1])

mental shear can be analyzed using:

$$\Delta u = c \quad (1.1)$$

where

$$c^2 = 2 \int_0^H (-B_L) dz \quad (1.2)$$

$$B_L = g \left[\frac{\theta'}{\bar{\theta}} + 0.61(q_v - \bar{q}_v) - q_c - q_r \right] \quad (1.3)$$

with c being the buoyancy of the cold pool and its related vorticity and Δu being the environmental shear related to the environmental vorticity[8]. Equation 1.1 can be used to study the vorticity balance with an “optimal state” being defined when they are equal, implying a vertical updraft as described by RKW (1988). In the buoyancy equation (equation 1.3), θ is the potential temperature, q_v is the mixing ration of water vapor, q_c is the mixing ratio of cloud vapor, and q_r is the mixing ratio of rain water which is examined across the cold pool boundary with the bars denoting the mean state and the primes denoting the perturbation. For further information on derivation details, one is refered to RKW (1988) and Weisman (2003).

Vorticity is generated by the horizontal buoyancy differences (right side of equation 1.1) associated with the cold pool and the warm inflow (equation 1.2) and the environmental shear (left side of equation 1.1). The balance of these two helps to explain the initial mechanisms that lead to the evolution of the enhanced RIJ, a key feature of bow echoes. Once a storm has initiated, the environmental shear dominates and causes the updraft to lean downshear seen in Figure 1.2.a. The horizontal buoyancy field associated with the updraft causes buoyantly generated vorticity, opposite in sign around the updraft. The positive vorticity of the environmental shear adds to the buoyantly generated positive vorticity to cause the updraft to tilt upshear. A cold pool has not developed at this point, so there is no cold pool generated buoyancy difference opposite in sign to that of the environmental shear vorticity to enable a balance and maintain a vertical updraft.

Once the cell has gone through its lifecycle and formed a downdraft and subsequent cold pool,

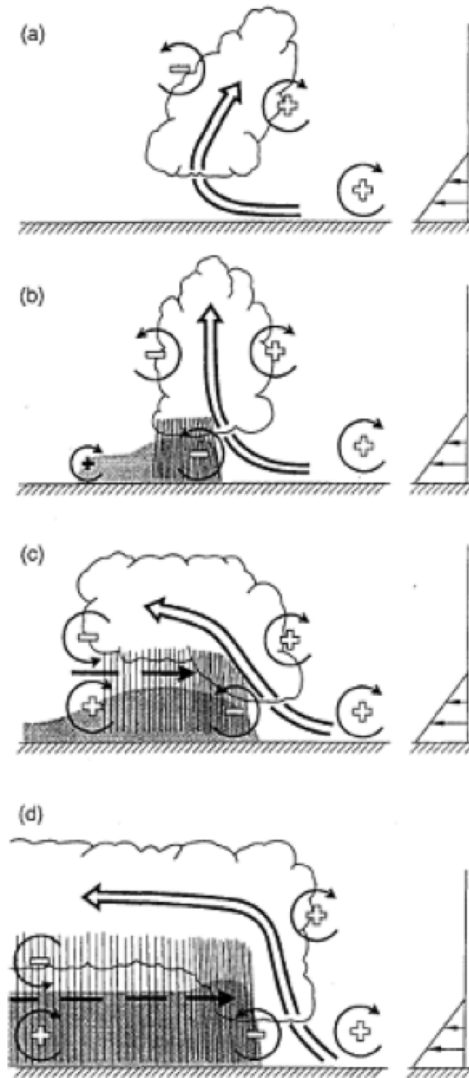


Figure 1.2. Bow echo cross-section evolution. (Source: Weisman 1993 [2])

a buoyancy difference between the cold pool and the warmer inflow air is set up. This allows for the buoyancy differences to generate vorticity (rising associated with the relatively warm inflow and sinking with the cooler cold pool) in the opposite sense and balance the environmental shear generated vorticity allowing the updraft to become more vertically erect as seen in Figure 1.2.b. This optimal balance between cold pool strength and the environmental shear, studied by RKW (1988), allows for the continuous propagation of the squall if it can be maintained and allows for continual formation of convective cells ahead of the propagating cold pool.

The cold pool continuously strengthens, being reinforced by the evaporatively cooled air from the downdraft. Once the cold pool and buoyancy gradient becomes too strong, it overtakes the environmental shear generated vorticity and causes the updraft to tilt rearward over the cold

pool. This can be seen in Figure 1.2.c. This is generally marked as the decay stage of a squall line since the upshear tilt generally produces shallower lifting along the leading edge as described in RKW (1988). A horizontal buoyancy gradient is subsequently generated at the rear end of the updraft aloft and the cold pool near the rear of the storm. This generates vorticity in the opposite sense in comparison with the front of the cold pool (sinking on the left/rising on the right compared with rising on the right/sinking on the left) ushering in a rear to front flow marked by the black lines in Figure 1.2.c. The tilted updraft behind and above the cold pool forms additional shear generated negative vorticity enhancing the RIJ ushered in by the horizontal buoyancy field generated vorticity in the opposite sense at the rear of the line. This RIJ formation can also be described by a hydrostatic pressure argument derived from a buoyancy-generated pressure field at mid-levels. This hydrostatic pressure field is caused by the difference between the gradient in the warm anomaly aloft causing an acceleration of rear mid-level air above the cold pool towards the front of the advancing cold pool.

Normally, the upshear tilted phase is the end of the lifecycle of the squall line, but it can be overcome by the formation of a strong RIJ that ushers in the bow echo phase. The strong RIJ remains elevated and helps generate shear vorticity in the opposite sense to that at the leading edge of the cold pool, counteracting the strengthened cold pool buoyantly generated vorticity near the front of the line. This allows for the balance of vorticity at the leading edge to be regained and the updraft again tilted vertically to allow deep lifting and new cell formation. Figure 1.2.d shows the new balance of vorticity with the enhanced RIJ counteracting the leading edge enhanced cold pool generated vorticity. The development of the elevated RIJ is also aided by the development of mid-level rotation that enhances the midlevel rear-inflow allowing for a bowing segment to form. This midlevel rotation has been commonly referred to as the “bookend vortices” [2].

The classic comma signature of bow echoes is produced by the “bookend vortices” [2]. The buoyantly generated horizontal vorticity is tilted vertically by the updraft and downdrafts [9]. The cyclonic and anti-cyclonic vertical vortex couplet associated with the tilted horizontal vorticity cause a region of enhanced midlevel flow between the pair providing a reinforcement of the RIJ along the central axis (up to $7\text{--}15\text{ m}\cdot\text{s}^{-1}$ in ideal situations) [2]. The magnitude of the reinforcement is dependent on the spacing and strength of the vortices. A smaller distance between the couplet members provide a stronger central axis wind.

The environmental conditions for bow echo genesis can vary depending on the synoptic forcing present. Two dominant conditions are found to exist: rapidly propagating squall lines associated with mid-latitude cyclones and slower propagating squall lines with relatively weak synoptic forcing. Johns and Hirt (1987) studied a dataset of 70 derechos, a more general definition for a line of severe wind producing complexes with dominant bowing features. Their derechos formed from 1980-1983 in the warm season (May–August). From the statistics compiled, it was found that almost two thirds of the events occurred in June and July, with almost 80% forming between 1600 and 0400 UTC [3].

Two patterns of bow echo propagation were found: progressive propagation and serial prop-

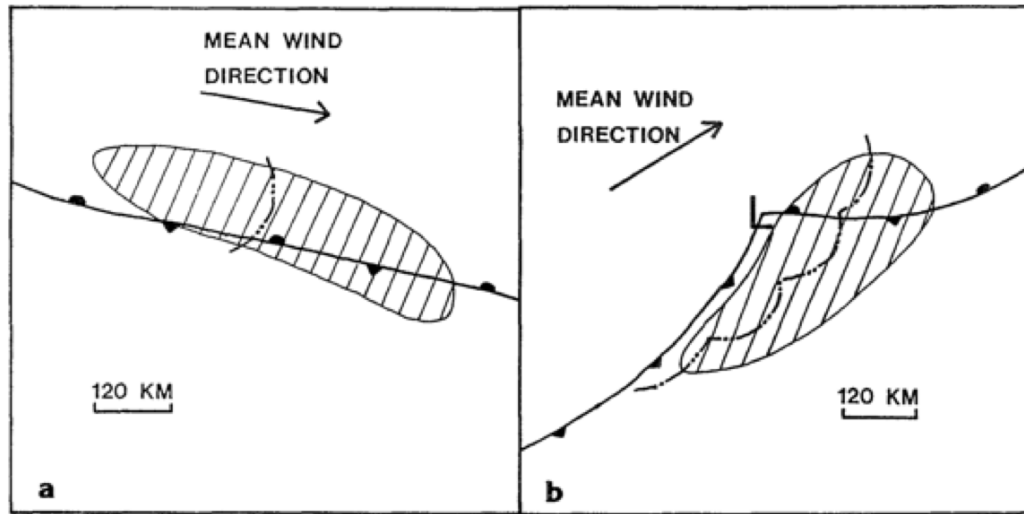


Figure 1.3. Bow echo propagation associated with synoptic pattern (a) weak forcing and (b) strong dynamic forcing. (Source: Johns and Hirt 1987 [3])

agation. Progressive lines are “characterized by a short curved squall line oriented nearly perpendicular to the mean wind direction with a bulge in the general direction of the mean flow[3]. These bow echoes traveled along a surface boundary with a study average speed of $23 \text{ m}\cdot\text{s}^{-1}$. More than half of the progressive bow echoes traveled faster than the mean wind indicating other important dynamic factors. Serial lines “involve a squall line oriented such that a relatively small angle exists between the mean wind direction and the squall line axis[3]. These structures move perpendicular to the surface boundary and generally involve a series of bow echoes as a part of a LEWP with a study average speed of $15 \text{ m}\cdot\text{s}^{-1}$ or less. These propagation schemes can clearly be seen in Figure 1.3[3].

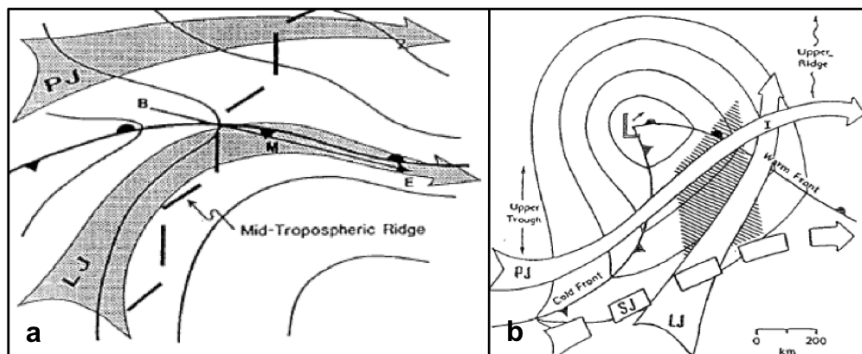


Figure 1.4. Synoptic environmental patterns (a) “weak forcing” and (b) “strong dynamic forcing”. (Source: Johns 1993 [4])

The synoptic pattern and surface features play a large role in the propagation and severity of the bow echoes. Over 86% formed along or to the north of some sort of surface boundary. With the strong synoptically forced pattern (Figure 1.4.b), bow echoes were found to form ahead

of quickly propagating low pressure systems aligned parallel to a trailing cold frontal boundary. The weakly forced pattern (Figure 1.4.a) was found to be associated with strong instability from low-level warm and moist advection converging along a quasi-stationary boundary[4]. This large moisture advection is typically correlated with the growing season in late spring and early summer with vegetation enhancing surface moisture in these regions and boosting the frequency and severity of warm season events[4]. The strong synoptic forcing patterns tend to produce serial propagating bow echo complexes while weaker, “warm season” patterns, tend to produce progressive propagation.

Stronger forcing allows for the formation of storms in stronger sheared environments with much less instability ($\text{CAPE} < 2000 \text{ J}\cdot\text{kg}^{-1}$). Their damaging surface winds are a result of the fast mean flow in which they are imbedded transferring horizontal momentum through the downdraft from higher upper levels to the surface[4]. The weakly forced systems tend to have stronger low-level system-relative inflows that indicate large propagation speeds due to their strong cold pools. These events occurred in much more unstable environments, and their cold pools were found to be stronger than their strong forcing counterparts, although this correlation was much weaker than the instability comparison. The cold pool plays a large role in the genesis and maintenance of the severe surface winds and downbursts along the bow echo and the generation of new cells along the gust front.

The squall line and subsequent bow echo during the 9-10 Jun 2003 BAMEX experiment followed the previously defined strong forcing pattern, although it has characteristics of both weak and strong. Large values of CAPE and 0-3 km low-level shear were present before and after convection initiation, which were very similar to the thresholds of CAPE and low-level shear determined by Weisman (1993) to be conducive for bow echo formation. The parameters were argued to be a necessary condition, but a study by James et al. (2006) found these may be necessary, but not sufficient conditions for bowing convection and focused on the moisture content of the low- and mid-levels on cold pool formation and strength[10]. This study looks at the minimum threshold requirements of CAPE and low-level shear, but future work will incorporate the findings of James et al. (2006) as another parameter to analyze for the ensemble members environment and the effect on bow echo formation.

1.1.2 BAMEX

The Bow Echo and MCV Experiment (BAMEX) was designed to provide valuable observations of bow echoes and mesoscale convective vortices (MCV) throughout their lifetime and at multiple scales. This experiment provided the most comprehensive data set to date for these types of MCSs, using both ground based and airborne mobile observations[11].

The experiment was conducted from 20 May to 6 Jun 2003 across the Midwest and high plains of the United States, with field headquarters at MidAmerica St. Louis Airport in Mascoutah, Illinois. The broad objective was to observe MCSs at scales ranging from those of the outflow boundaries and rear inflow jets of squall lines and bow echoes to the larger MCVs and

environmental structure[11]. The scientific objectives included improving predictability of bow echo disturbances and secondary convection generated by mesovortices, documenting and understanding horizontal circulations in long-lived convective systems, and improving Quantitative Precipitation Forecasts (QPF) for the 6-24h timescale[12].

To accomplish this task, many instrumented aircraft and ground instruments were deployed within the BAMEX domain. The aircraft included the NOAA P-3, NRL P-3 with ELDORA (Electra Doppler Radar), and a lear jet leased from Weather Modification, INC. The ground teams included MIPS (Mobile Integrated Profiling System), MGLASS (Mobile GPS/Loran Atmospheric Sounding System), and mobile probes. The combination of the ground and airborne instruments allowed detailed thermodynamic profile soundings, dropsondes soundings, and surface in-situ measurements of the event along with high-resolution spatial and temporal Doppler sampling providing dual and quad-doppler analyses of the storms. After storms had passed through a region, damage survey crews used detailed areal photography to provide a damage survey of the regions[11].

During the field campaign, 18 successful missions (termed IOPs or intense operating periods) were performed, providing the most comprehensive data set to date for these MCSs. The 9-10 Jun 2003 case was one of these successful missions (IOP 7A) with extensive Doppler coverage both from aircraft and WSR-88Ds. Multiple sampling platforms provided high-resolution quad-Doppler analysis for a large portion of the southern bow passing over Lincoln Nebraska. The Learjet dropped 31 dropsondes throughout the progression of the system, with MIPS and MGLASS providing an extensive pre- and post-environmental thermodynamic data set[11].

1.1.3 Predictability

The sensitivity of squall line and bow echo formation and lifecycle to stochastic convective processes has a large impact on the predictability of these events. In numerical weather prediction, the initial conditions can play a large role in the evolution of the forecast. Forecasts are very sensitive to small differences in these initial conditions and, in principle, continually improving the initial conditions will increase predictability. This was discounted by Lorenz in 1969 who conjectured that the errors inherent in the initial conditions would grow more rapidly as the initial conditions were improved and smaller scales were resolved[13]. In his argument, faster error growth would put a finite limit to the predictability of the atmospheric state. Therefore, each successive improvement in the initial conditions would yield smaller improvements in the predictability until a limit was reached.

In a larger context, there are two types of predictability, practical and intrinsic. Practical predictability is defined as “the ability to predict based on the procedures currently available”[14]. Intrinsic predictability is defined as “the extent to which prediction is possible if an optimum procedure is used”[13]. The practical predictability can be limited by uncertainties in both the forecast model and initial conditions that are not infinitesimally small and are a byproduct of current technological capability. The intrinsic predictability is the predictability given per-

fect knowledge of the atmospheric state and a perfect forecast model, which is technologically infeasible[13].

A multitude of past studies have examined the predictability of mesoscale features starting with Anthes et al. (1985) looking at the forecast divergence of simulations of different initial conditions in a limited area mesoscale model. This study found unreasonably slow forecast divergence that was later found by Errico and Baumhefner (1987) as being due to the use of fixed boundary conditions, unbalanced initial perturbations, and strong numerical dissipation[15]. More recently, Zhang et al. (2002) studied the possible reason for forecast success during a “surprise snowstorm on the 24-25 of January 2000” looking at various sensitivity experiments. Through these experiments it was found that insufficient model grid resolution, poor interpolation of a few key soundings during data assimilation, and errors in the initial conditions caused significant problems in the simulated forecasts. Small initial condition alterations by removing sounding data led to differences in 24 to 36 h mesoscale precipitation distributions. The experiments also alluded to forecast differences from the rapid error growth associated with moist processes on smaller scales (< 500 km)[16].

A subsequent study of the moist processes associated with the Zhang et al. (2002) storm through various simulations of a high-resolution mesoscale model was performed by Zhang et al. (2003). The goal was to look at moist convection as the primary mechanism for forecast-error growth at smaller scales. It was found that small-scale error from moist process below 100 km rapidly grew upscale. These error growths were associated with the non-linearity inherent with the microphysical and parameterization schemes. Significant differences were found in the timing and position of individual cells on short time scales ($O(1 \text{ h})$), causing a predictability limit of larger scales from the upscale error growth associated with the convective cells. Through sensitivity studies, it was shown that the rate at which this error grows upscale is increased as the initial condition error amplitude is decreased [17].

A study by Tan et al. (2004) conformed with Zhang et al. (2003) findings. In the Tan et al. (2004) study, the error growth associated with idealized baroclinic waves in a conditionally unstable atmosphere was analyzed[18]. They found that without the effects of latent heating, error growth was small from 0-36 h, but when the latent processes were included, errors grew rapidly upscale.

Zhang et al. (2006) took the previous findings and explored the intrinsic and practical aspects of a warm-season flooding event. The goal was to find the fundamental processes that controlled the predictability and error growth within the simulations. Using various sensitivity studies it was found that the initial condition uncertainty and inherent model error lead to large forecast errors. Also, small-amplitude, large-scale errors can grow rapidly and contaminate the short-term deterministic mesoscale forecast[14].

Zhang and Bei (2007) applied the previous concepts and methods to an extreme flooding event along the Mei-Yu front in China. The goal of the study was to analyze the effect of perturbations of different scales to the predictability of the precipitation. Similar findings to Zhang et al. (2002), (2003), and (2006) were found, with small-scale error growth being strongly

nonlinear and rapid upscale growth due to moist processes. Applying initial perturbations to various scales produced similar forecasts given that the initial condition error was small. It was concluded that the mesoscale predictability of the flooding event was inherently limited[19].

Ensemble forecasts have proven useful for forecasting many atmospheric phenomena ranging from tropical cyclones to MCVs. A more recent study by Hawblitzel et al. (2007) used an ensemble to look at the dynamics and predictability of an MCV that formed during the BAMEX campaign. They found that small-amplitude, large-scale initial perturbations resulted in a large ensemble spread, with some members forming a very strong MCV while others formed no MCV at all. It was determined through correlations of environmental fields and midlevel potential vorticity that the strong MCV members had stronger and widespread convection 24 h before the MCV developed. The vast differences in ensemble members was determined to be caused by moist convection, with the upscale error growth causing significant forecast uncertainty[20].

Ensemble forecasts were also used in a recent study by Sippel and Zhang (2009) to examine the effects of small amplitude variations in initial conditions on the predictability and structure of a tropical cyclone. They also found that the predictability was limited due to the effects of moist convection[21]. The small, essentially unobservable initial condition differences in temperature, wind, moisture, and pressure in the study led to different routes in tropical cyclogenesis, with some members forming strong tropical cyclones while other members formed none. The divergence in the solutions was found to be caused by the chaotic interactions of mesoscale cold pools whose location, intensity, and timing altered the route of tropical cyclone formation. The cold pools dependence on small-scale convection and the chaotic differences between convective cells within the members caused large-scale forecast uncertainty.

1.2 Study Objective

In this study, a similar approach to Hawblitzel et al. (2007) and Sippel and Zhang (2009) is applied to the 9-10 Jun 2003 bow echo and squall line event. Done et al. (2004) suggested that the high-resolution WRF model run during the BAMEX campaign for field forecasts were able to simulate the timing, location, and mode of a majority of the MCSs encountered. The success of the WRF deterministic forecast during the BAMEX campaign suggested that deterministic numerical weather prediction of convective scale processes had come to fruition. This study examines one of these storms using an ensemble with realistic initial conditions test this claim. Comprehending the mesoscale predictability and corresponding error growth dynamics of mesoscale forecasts is fundamental for advancing deterministic mesoscale forecasts, thus providing guidance on the design and implementation of ensemble prediction systems[14].

The predictability of the event, both practical and intrinsic, are examined through various methods of ensemble analysis. The variability of convection in the ensemble, both spatially and temporally, is used to highlight the practical predictability. Averages of good and poor members within the ensemble are used to simulate improving the initial conditions to study the intrinsic predictability. Similar sensitivity studies to Bei and Zhang (2007) and Zhang (2002) are applied

to the reduced initial condition deterministic forecasts to study the effects of moist processes on small-scale error growth and their effect on large scale forecast divergence. Basic severe weather parameters to forecast squall line and bow echo strength 18 to 24 h into the forecast are compared among model members.

To get a more detailed examination of this convective event, an overview of the synoptic environment and storm-scale evolution is presented in Chapter 2. A description of the model employed and the ensemble and initial conditions are described in Chapter 3. The practical predictability and ensemble variability are described in Chapter 4, subjective classification of ensemble members and severe weather parameter forecasting analysis is in Chapter 5, and the intrinsic predictability with simulated reduction in ensemble spread is in Chapter 6. Concluding remarks can be found in Chapter 7.

Chapter 2

Case Overview

2.1 Synoptic Environment

During the 24-h period of 9-10 Jun 2003, the northern BAMEX region was characterized by a weak 300-hPa westerly jet stream extending across the high plains and into the Ohio river valley with predominantly zonal flow. An embedded shortwave trough over eastern Montana

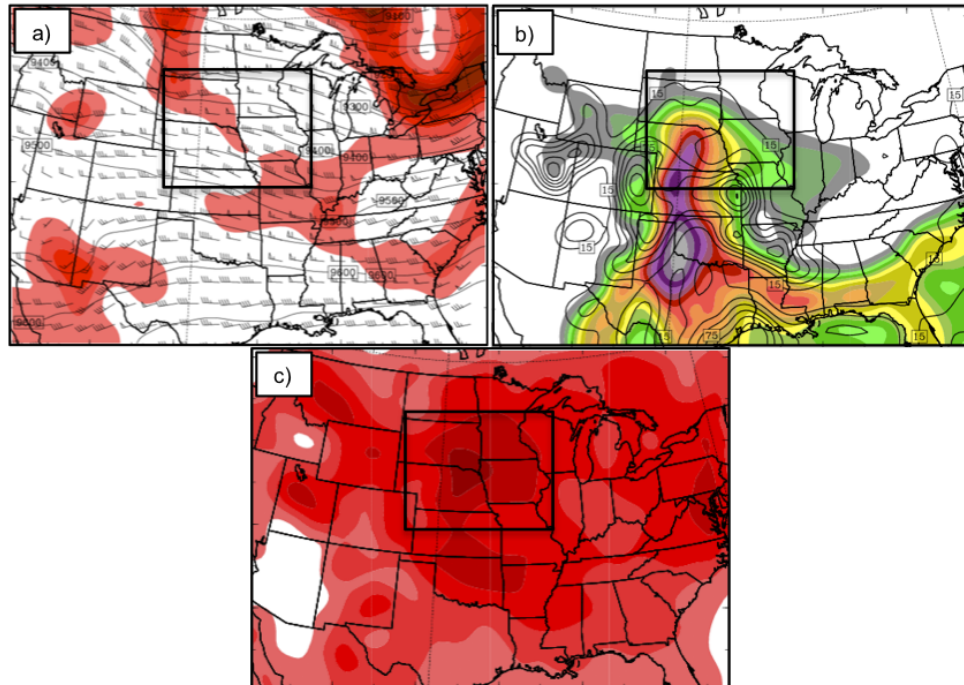


Figure 2.1. FNL analysis valid 0000 UTC 10 Jun 2003 (a) 300-hPa PV (shaded every 0.5 PVU), height (every 50 m), and wind (full barb $5 \text{ m}\cdot\text{s}^{-1}$) (b) most unstable CAPE (shaded every $250 \text{ J}\cdot\text{kg}^{-1}$) and most unstable CIN (contoured every $20 \text{ J}\cdot\text{kg}^{-1}$) (c) 0-5km bulk shear (shaded every $3 \text{ m}\cdot\text{s}^{-1}$). The box in (a-c) denotes the high resolution 3.3 km domain.

at 1200 UTC 9 June (Figure 2.1) migrates over the northern BAMEX region by 0000 UTC 10 June providing synoptic destabilization. A 250-hPa jet streak ahead of the shortwave by 0000 UTC June 10 aligns its right entrance region over southern South Dakota and northern Nebraska providing additional synoptic scale lift. At the surface, low pressure develops ahead of the approaching shortwave, strengthens on the eastern side of the Rocky Mountains in eastern Wyoming, and moves over western Nebraska by 2100 UTC 9 June. A trough extends southwest into eastern Colorado. A southerly 850-hPa low level jet (in excess of 40-knots) extends through central Kansas and Nebraska ahead of the surface trough (Figure 2.2), advecting dewpoints in excess of 60° F into northern Nebraska. The southerly low level jet (LLJ) and zonal flow aloft

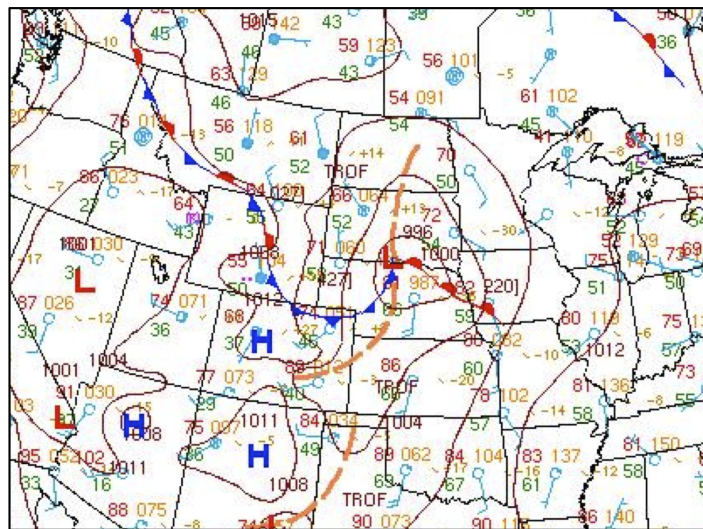


Figure 2.2. Hydrological Prediction Center (HPC) surface analysis valid at 0000 UTC 10 Jun 2003.

provide strongly veering hodographs indicated by the 0000 UTC 10 June OAX sounding (40-knot 0-6 km shear) conducive for supercell and squall line development. Strong moisture advection with the aid of the LLJ leads to CAPE in excess of $3000 \text{ J}\cdot\text{kg}^{-1}$ over central Nebraska. The circulation associated with the surface low brings drier continental air from the northwest and moisture from the Gulf of Mexico from the south which builds a tight moisture gradient (dry line) that extends from northwestern Kansas into south central South Dakota by 2200 UTC 9 Jun. The dryline provides a region of surface convergence extending into the surface low circulation.

2.2 Mesoscale Evolution

By 2100 UTC 9 Jun, the BAMEX radar composite shown in Figure 2.3 indicates convective development over south central SD, with discrete supercell development over Holt County, Nebraska. Another supercell is found at 0000 UTC 10 Jun over Custer county, Nebraska. By 0100 UTC 10 Jun, both supercell storms had reports of strong tornadoes, sizable hail, and damaging surface winds. The discrete cells moved southeastward, with the northern cell developing into a

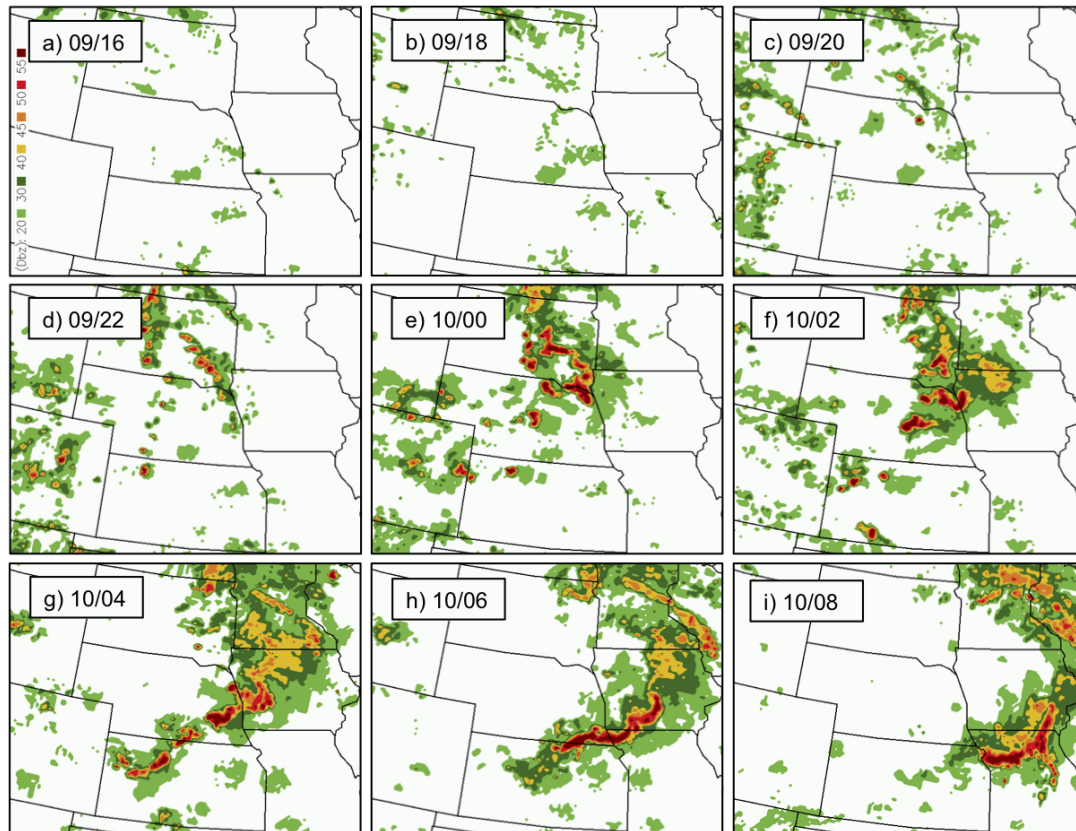


Figure 2.3. Composite radar reflectivity (dBz) observed at (a) 1600 (b) 1800 (c) 2000 (d) 2200 UTC 09 Jun 2003; (e) 0000 (f) 0200 (g) 0400 (h) 0600 (i) 0800 UTC 10 Jun 2003.

bowing line segment by 0300 UTC 10 June and the southern cell shortly following. Numerous reports of damaging surface winds in excess of 70-mph near Lincoln and Omaha were reported to the local NWS weather office between 0300-0600 UTC 10 Jun. The two discrete cells merged into one 350 km bowing line structure over southwestern Iowa by 0600 UTC 10 Jun.

Chapter 3

Experimental Design

3.1 Model Description

This study utilizes the fully compressible, non-hydrostatic mesoscale Weather Research and Forecasting Model (WRF) version 2.2 with ARW (Advanced Research WRF) core dynamics. The forecast model is initialized at 1200 UTC 09 Jun 2003 and integrated for 24-h. Four domains are employed, three of them two-way nested, with horizontal grid spacing of 90, 30, 10, and 3.3 km, respectively, as indicated in Figure 3.1. The course domain (D01) encapsulates the entire

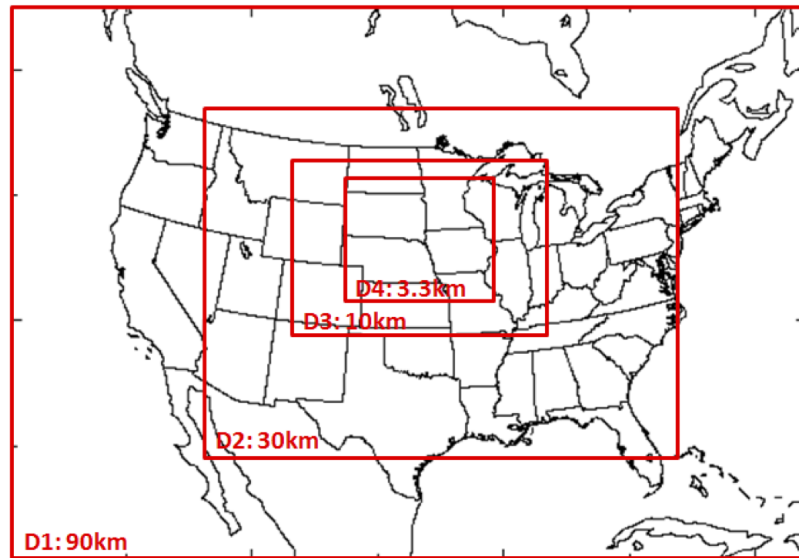


Figure 3.1. Schematic of domains used in the study.

CONUS, with subsequent domains honing in on the BAMEX region of interest. The two domains with horizontal grid spacings of 30 and 3.3 km (from here on D02 and D04), use horizontal grid points of 115 x 82 and 258 x 297, with the high-resolution D04 indicated by the black box in

Figure 2.1. D04 is intended to cover the BAMEX region of interest to capture the evolution of the supercell and subsequent bow echo and squall line. All four domains utilize 27 vertical terrain-following sigma levels, the WRF Single Moment (WSM-6) six-class microphysics scheme with graupel[22], and the Yonsei State University (YSU) planetary boundary scheme[23]. Given the course resolution of D01, D02, and D03, the Grell-Devenyi cumulus scheme[24] is employed. D04 is both convective permitting and convective resolving for the convection of interest with this study, hence has no cumulus parameterization[25].

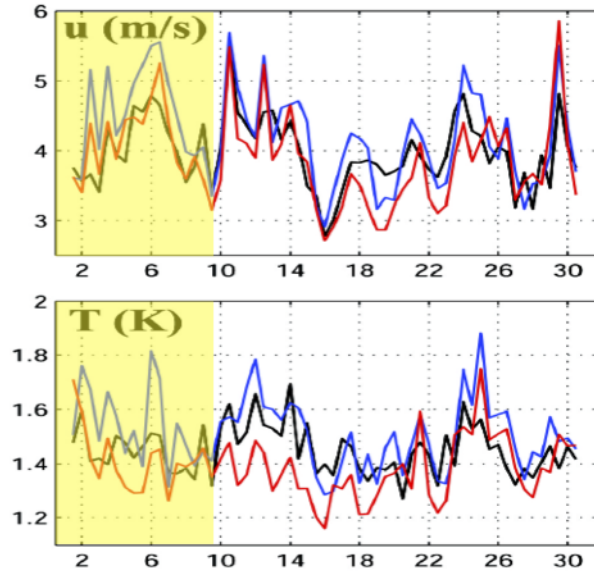


Figure 3.2. Root mean square error in temperature (K) and zonal wind ($\text{m}\cdot\text{s}^{-1}$) from the Meng and Zhang 2008[5] month long experiment between EnKf (red), WRF-3DVar (blue), and FNL-GFS (black). (Source: Meng and Zhang (2008) [5])

This study utilizes a 40 member ensemble generated during a month-long data assimilation experiment covering June 2003 by Meng and Zhang (2008)[5]. That study looked at the performance of EnKF versus WRF-3DVar data assimilation to find general comparisons on regional scales. Figure 3.2 highlights the root mean square error for zonal wind component ($\text{m}\cdot\text{s}^{-1}$, top panel) and temperature (K, bottom panel) between the EnKF, WRF-3Dvar, and FNL-GFS forecast (a 12 hour forecast from the FNL analysis interpolated to the WRF grid with the same model configuration as the WRF-3Dvar) for the entire month of June compared to quality controlled rawindondes at nine pressure levels located in the BAMEX region. Both panels indicate overall better performance of the EnKF with similar results for other prognostic variables (not shown). On 9 Jun, the EnKF analysis has low root mean square error, below both the WRF-3Dvar and the FNL-GFS analysis in T , u , and q , indicating an accurate representation of the atmospheric state.

3.2 Ensemble Initialization

The 40 members were initialized at 0000 UTC 01 Jun 2003 and subsequently run for the month of June 2003. The National Center for Environmental Prediction (NCEP) final analysis (FNL) was used to define the initial and boundary conditions. The FNL-GFS analysis is a gridded dataset from the GFS (Global Forecasting System) global spectral data assimilation and forecast model system providing atmospheric variables at 26 vertical levels at a horizontal resolution of 0.5 degrees every 6 hours. The initial ensemble was generated from the WRF-3DVar[26] using the climatological background error covariance at 0000 UTC 01 Jun 2003 to create balanced perturbations in the temperature (T), horizontal wind components (u and v), water vapor mixing ratio (q), and pressure (p). The perturbation standard deviations generated were approximately 1 K for potential temperature, $2 \text{ m}\cdot\text{s}^{-1}$ for horizontal wind components, $0.5 \text{ g}\cdot\text{kg}^{-1}$ for the water vapor mixing ratio, and 1-hPa for pressure[5], values which are smaller than operationally employed perturbations used in NCEP ensemble initialization. Randomly selected WRF-3DVar balanced perturbations are added to the FNL analysis to generate 40 ensemble members and integrated for 12 h before the data assimilation cycle is started to generate a flow-dependent background error covariance for the EnKF. To provide a reasonable perturbed lateral boundary for D02 during the experiment, D01 boundary conditions are updated every 12 h using the same technique to generate the initial conditions (from the FNL-GFS analysis). This cycle is shown in Figure 3.3. Following the schematic, the initial ensemble with applied FNL-GFS balanced

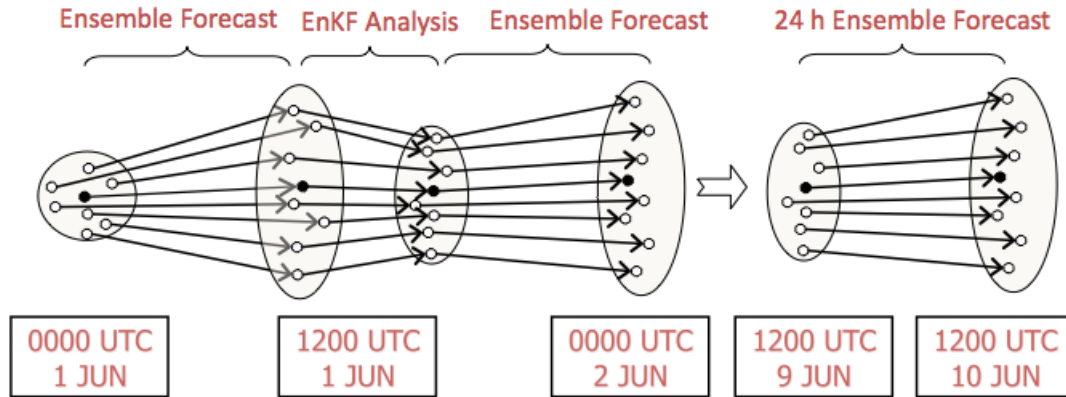


Figure 3.3. EnKF data assimilation cycle schematic.

perturbations is run for 12 h. The observational data is subsequently assimilated with the EnKF using the flow-dependent background error covariance derived from the ensemble. The analysis is then integrated 12 h and the process repeated. Data assimilation of observations are only performed in D02 using sounding, wind profiler, and surface observations every 12 h. The results are compared against quality controlled BAMEX rawinsondes at nine pressure levels for verification. (For further information on the data assimilation, observation quality control, and verification techniques, one is directed to Meng and Zhang (2008b)[5].)

After the data assimilation process is repeated multiple times, the ensemble forecasts for this study are initialized from the 1200 UTC 9 Jun EnKF analysis ensemble members. Each member is integrated for 24 h to 1200 UTC 10 Jun 2003 using the WRF-ARW model with no data assimilation during the period (each member is a deterministic forecast).

Chapter 4

Ensemble Variability, Error Growth, and Practical Predictability

The WRF model was used during the BAMEX campaign to provide high-resolution forecasts of the region. Many of the forecasts did very well in predicting the mode, temporal, and spatial characteristics of many storms during BAMEX, of which the Jun 9-10 2003 performed exceptionally well. The good performance by the WRF deterministic forecast led to an impression that deterministic convective-scale numerical weather prediction had arrived. This chapter looks at the variability of an ensemble with small initial condition error, below current observation standards. The variability that ensues highlights the limit of practical predictability for this case.

4.1 Ensemble Variability

The 40-member ensemble derived from the EnKF provided a wide variety of results given the small ($\approx 2 \text{ m}\cdot\text{s}^{-1}$) initial ensemble spread, indicated in Figure 4.11.a. A mosaic of 20 members depicting D04 over the BAMEX region at 0600 UTC on Jun 10 is shown in Figure 4.1. These simulated reflectivity fields are 16 h into the forecast. This time was chosen for the mosaic since it shows the best (subjectively chosen) representation of the different storm modes within the ensemble. From top left to bottom right, the images show an assortment of members ranging from full squall lines with bowing sections to back building mesoscale convective systems with chaotic disreect cell arrangement. The selection is a representative sample of the various storms in the ensemble. Analyzing the members and modes of the mosaic indicate that the model is capable of producing a realistic and representative storm mode with similar structure, spatial coverage, and temporal phasing to the observations. Many members produced strong squall lines, but they

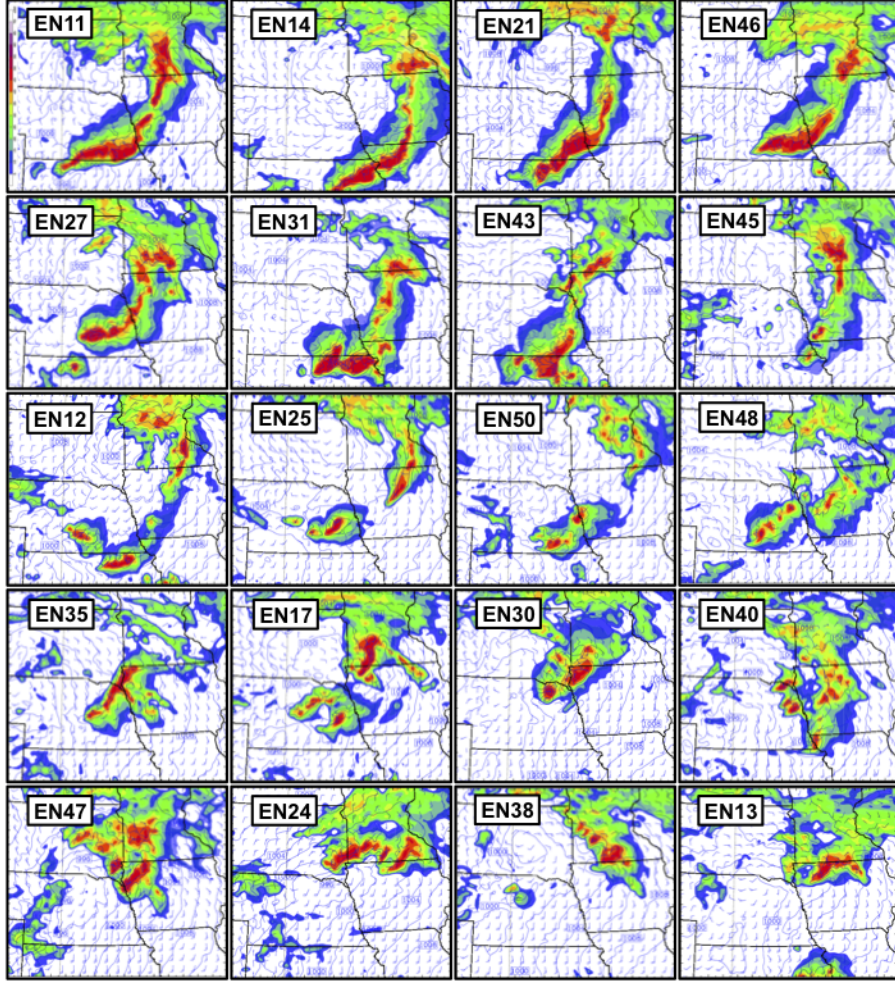


Figure 4.1. Simulated radar reflectivity (dBZ), sea level pressure (hPa), and surface winds (full barb 5 $\text{m}\cdot\text{s}^{-1}$) for 20 ensemble members at 0600 UTC 10 Jun.

were out of phase with observations in terms of their spatial location or temporal progression of the line. The model also is capable of producing members that do not produce squall lines at all, but instead generate lines of discrete propagating cells, back-building mesoscale convective systems, and small convergent convective lines that had slight bowing characteristics. The low spread of the initial conditions and striking variability in storm mode is a strong indicator of a chaotic divergence of the ensemble members and hints at multiple flow regimes.

Generally, the ensemble mean is considered the most likely representation of the ensemble and provides the theoretical most likely outcome. Figure 4.2 shows two variations at 0600 UTC 10 Jun of the ensemble mean, one using the ensemble mean for D01 and EnKF analysis for D02 and the other the FNL analysis for D01 and EnKF analysis for D02. Also, a deterministic WRF forecast using purely the FNL analysis for D01 and D02 is shown on the right for reference. The two similar ensemble means (both using the EnKF analysis for D02) indicate a squall line

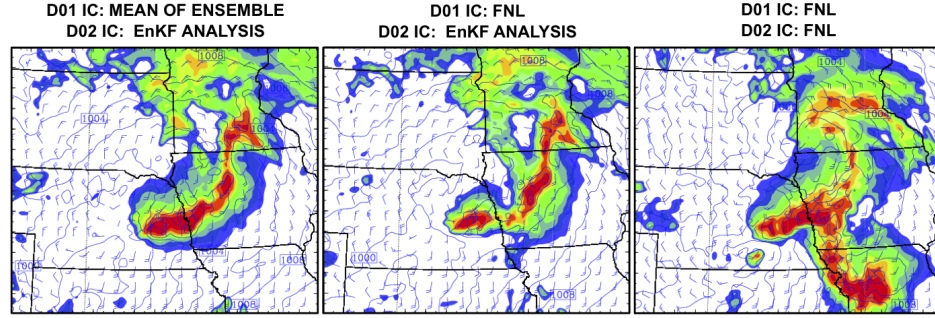


Figure 4.2. Simulated radar reflectivity (dBZ), sea level pressure (hPa), and surface winds (full barb $5 \text{ m}\cdot\text{s}^{-1}$) for initial conditions from ensemble mean and EnKF analysis (left), FNL and EnKF analysis (middle), and purely FNL analysis (right) at 0600 UTC 10 Jun.

and bowing feature, while the purely FNL analysis shows hints of a squall line, but clearly has a different outcome. For this study, the ensemble mean performed very well, producing a squall line and bowing structure, but did not spatially and temporally embody the squall line development as well as the “good members”. It was premature with squall line development and did not encompass the full line spatially. Therefore, the ensemble mean was not considered in further analysis, but good members that had better representation of observation were considered the best outcome from the model.

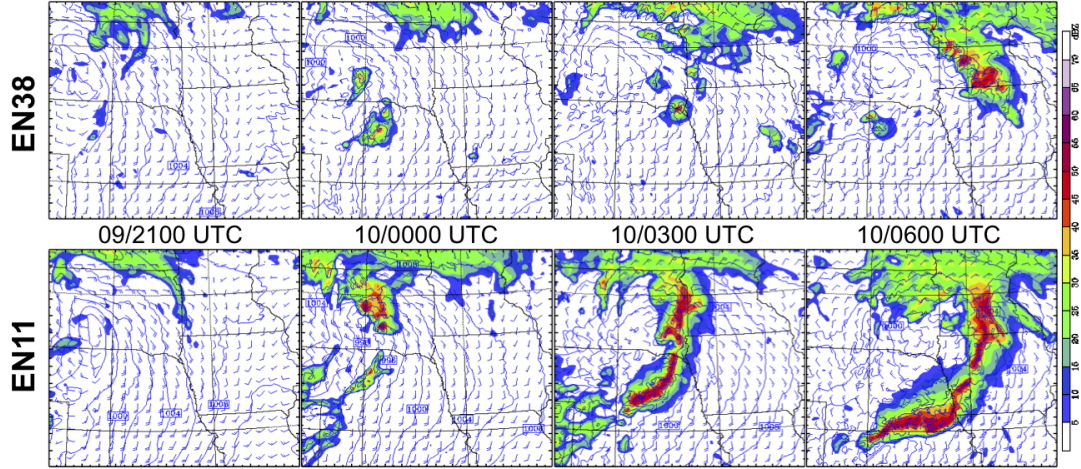


Figure 4.3. Simulated radar reflectivity (dBZ), sea level pressure (hPa), and surface winds (full barb $\text{m}\cdot\text{s}^{-1}$) for (a) EN38 and (b) EN11 from 2100 UTC 9 Jun to 0600 UTC 10 Jun.

With such variability in the members, not one consistent measure to classify storm strength, mode, spatial coverage, and temporal placement was easily derived. A subjective analysis of the members was performed with multiple iterations, each subsequent iteration incorporating more detail based on the previous iterations shortcomings, to derive a coherent scheme. The final criteria subjectively compared to observation for each member was decided to be storm mode (squall line, bowing structure and number of bows, other MCS), spatial phasing, temporal

phasing, and simulated reflectivity coverage northeast of the surface low. Multiple human participants applied this criterion to all ensemble members and a consensus was compiled with a final subjective ranking of good, fair, and poor. After ranking the members, a subsequent grouping into 10 good, 20 fair, and 10 poor was performed to focus the analysis on the 10 best and 10 worst representations of the actual storm, identifying the two storm modes. The mosaic of Figure 4.1 begins with 5 randomly selected good members, ends with 5 randomly selected poor members, and fills the middle with 10 randomly selected fair members. Clearly, the subjective analysis provides an effective method of classifying the ensemble members representative of observation.

Comparing a good and poor member of the ensemble is shown in Figure 4.3, EN11 with a strong squall line and bow echo and EN38 with back-building MCS development show two separate storm evolutions characteristic of many other members in the ensemble. The four-panel diagram shows a temporal evolution from convective initiation in north central Nebraska and south central South Dakota every 3 h until 0600 UTC when a clear squall line and bow echo form in member EN11 while member EN38 develops a line of discretely propagating convective cells. Given convective initiation between the surface warm front and the dryline for both cases, somewhere in the evolution, particularly between 0000 UTC and 0200 UTC Jun 10, a clear divergence in solutions occurs indicating two distinct flow regimes. These regimes were caused by differences in upper-level trough location and strength causing a cascade of environmental differences that eventually altered surface moisture and wind profiles. These evolution differences are evident in the distinction between good and poor members throughout the entire ensemble.

Zooming out into D02, covering a larger portion of CONUS, a shortwave over Montana at 1200 UTC Jun 9 in the initial analysis fields, evident in Figure 4.4.a as a trough over the southern Montana region, is determined to be an initial driving force behind the latter storm variability between ensemble members. A wide variety of trough structure exists in terms of both the strength and temporal placement of the trough axis as indicated by the large spread of the 500-hPa height lines. The spread in shortwave strength over the Montana region progresses through the 9 h prior to convective initiation, producing significant variability in the strength of the surface low over the northern Nebraska region. The differences in shortwave trough strength and temporal placement cause surface low evolution differences with higher amplitude shortwaves producing stronger lift, stronger surface low development, and a cascading effect on local gradients of surface winds, vertical wind shear, temperature gradients, and moisture gradients. The variable strength and surface placement of the low at convection initiation and the associated extended trough in the southwest Nebraska and northeast Colorado region are key factors in the divergence of the ensemble members into separate storm modes from differing environments.

Figure 4.5 shows an average environment for 10 subjectively chosen good and poor members from 2100 UTC 9 Jun. The top panels (a) indicate the 0.5 km parcel CAPE, the middle panels (b) indicate the 850-hPa winds and thus the LLJ, and the bottom panels show the 0-3km bulk shear. Larger CAPE, 850-hPa winds, and 0-3km shear are present near the convection initiation of interest in the good members (black star in Figure 4.6) compared with the poor members whose CAPE, 850-hPa winds and shear are weaker and displaced further south and east.

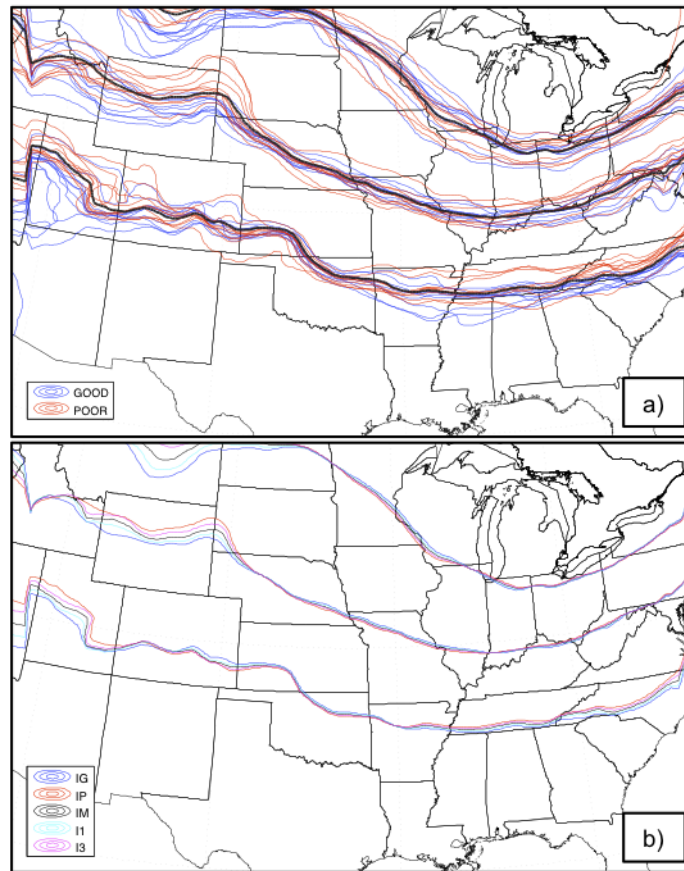


Figure 4.4. Pressure contours (525-, 530-, 535-hPa) on a 5.5 km constant height surface at 1200 UTC 9 Jun 2003 for (a) 10 good and 10 poor subjectively ranked ensemble members and (b) averaged deterministic ensemble members IG, IP, IM, I1, and I3.

Owing to the difference in the shortwave trough in both strength and temporal progression of the trough axis, a different environmental setup was present between the good and poor flow regimes. Figure 4.6 displays an environmental schematic representative of the good and poor environments with CAPE, CIN, 0-3 km bulk shear, low level jet (LLJ), sea level pressure, and surface boundaries highlighted at 2100 UTC 9 Jun with the black star indicating convection initiation of the storms of interest. The differences in some fields are smaller than others, but the placement of the surface low and related pressure field is probably the primary driving force of the surface winds and moisture advection. The good environmental setup has the surface low farther to the northeast with a tighter packing of isobars across southern South Dakota. The stronger initial low and cascading effect of stronger southerly winds advected larger CAPE values farther north. The poor environmental setup has a weaker upper level trough farther west, which caused a weaker and farther southwest placed surface low. This weaker surface low and further west placement is the most likely culprit of causing a weaker southerly jet, moisture advection, and larger CIN field (most likely caused by upper-level overrunning ahead of the warm front) to

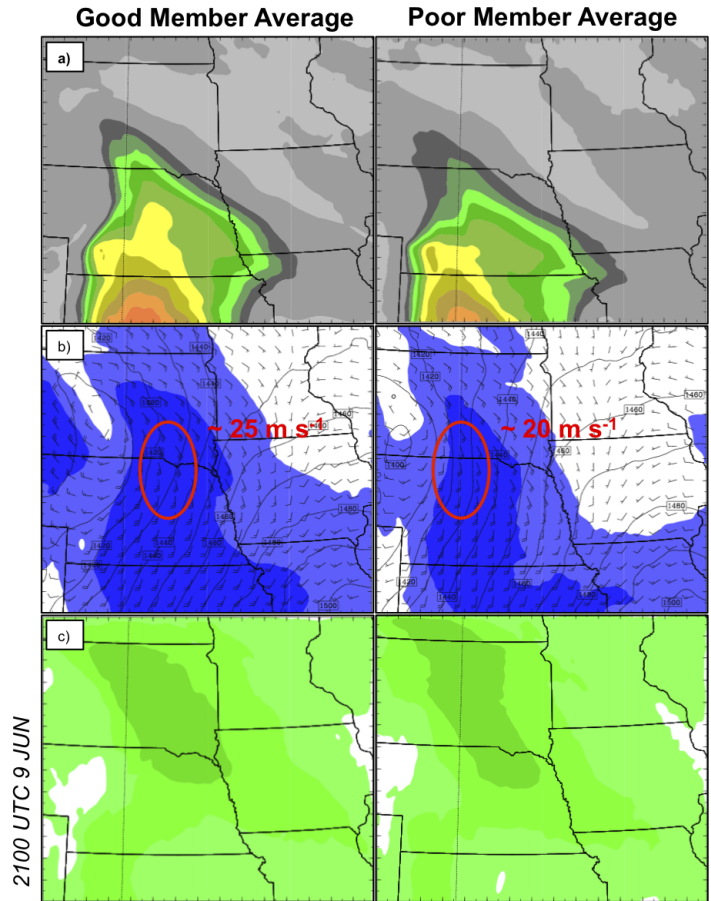


Figure 4.5. Average environment for good and poor members at 2100 UTC 9 Jun indicating (a) 0.5km CAPE ($\text{J}\cdot\text{kg}^{-1}$); (b) 850-hPa winds ($\text{m}\cdot\text{s}^{-1}$), heights (m), and wind speed (shaded, $\text{m}\cdot\text{s}^{-1}$); (c) 0-3 km bulk shear ($\text{m}\cdot\text{s}^{-1}$).

the northeast of the surface warm front at the time of convection initiation. Figure 4.7 displays the good and poor ensemble average soundings at the black star initiation points in Figure 4.6 to characterize the environment before convection initiation. Many similarities exist between members, but differences in the vertical wind profile and upper level moisture are present. From the sounding, the good members have stronger surface winds (20 knots), 700-hPa winds (30 knots) compared to the poor members surface (10 knots) and 700-hPa winds (20 knots). The mid-levels are drier for the good members enabling the possible development of stronger cold pools to balance the environmental shear and presumably produce a squall line mode. The increased moisture in the mid-levels would possibly hinder strong cold pool development in the poor members, causing weaker cold pools in conjunction with weaker environmental shear resulting in multi-cell development.

Figure 4.8 shows an average environment for 10 subjectively chosen good and poor members from 0200 UTC 9 Jun (same members as Figure 4.5). The top panels in Figure 4.8 indicate

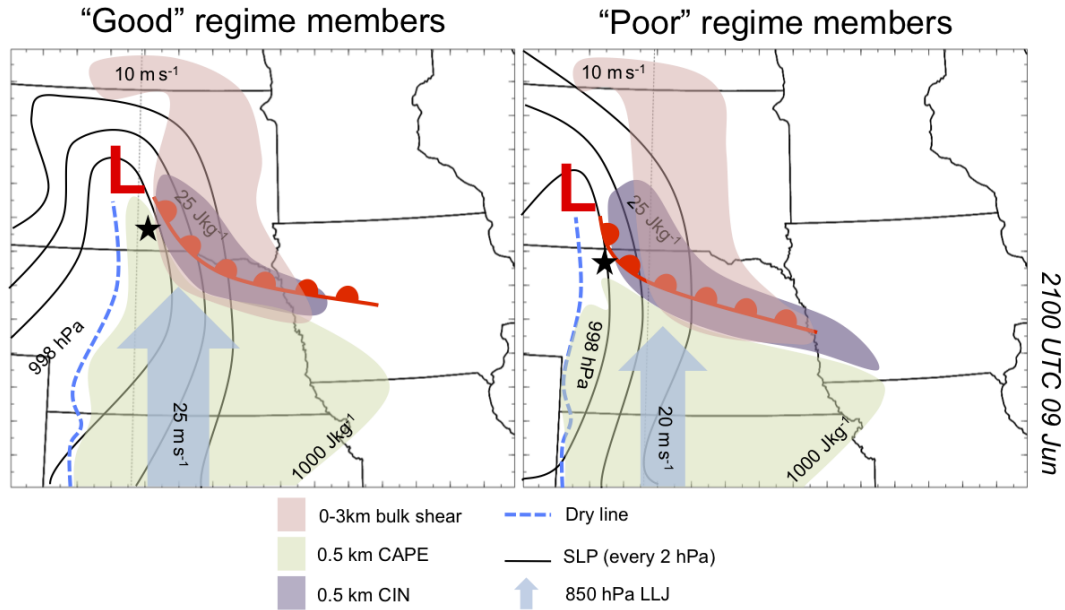


Figure 4.6. Schematic of environmental setup for the good and poor members at the time of convective initiation, 2100 UTC 9 Jun 2003.

the composite simulated reflectivity, sea level pressure, and surface winds, the middle panels (b) indicate the 850-hPa winds and thus the LLJ, and the bottom panels (c) show the 300-hPa PV and height fields. The simulated reflectivity panels clearly show a difference in convection by 0200 UTC with the good members clearly indicating a squall line with convection moving out of eastern Colorado merging along the southern flank. The poor members lack this southeast convection and the northern reflectivity region has indications of discrete convective cells, not a squall line. The 850-hPa winds (Figure 4.8.b) are much stronger ahead of the squall line in the good members, 40 knots from the southwest, versus the poor members that have a more southerly component with a jet of 30 knots. The upper-level shortwave in Figure 4.8.c and associated PV is much stronger for the good members than the poor members indicated by the evident trough and PV differences.

Figure 4.9 displays a representation of the good and poor members at 0200 UTC 10 Jun, the time when a strong difference in storm development and environmental conditions are evident. The good members have a stronger squall line reflectivity structure with a southern flank building to the south along the dryline with the leading convection oriented almost perpendicular to the strong low-level jet and CAPE. The poor members have weaker development in the northern sector with no convection along the southern extent of the dryline. The low-level jet and surface low position with convection ahead of the dryline in the poor members cause the surface winds to intersect the convection on the southern and western flanks of the southernmost cells. This allows for a back-building development without the aid of a surface boundary to aid in linear development. These flow differences are due to the upper level trough strength differences de-

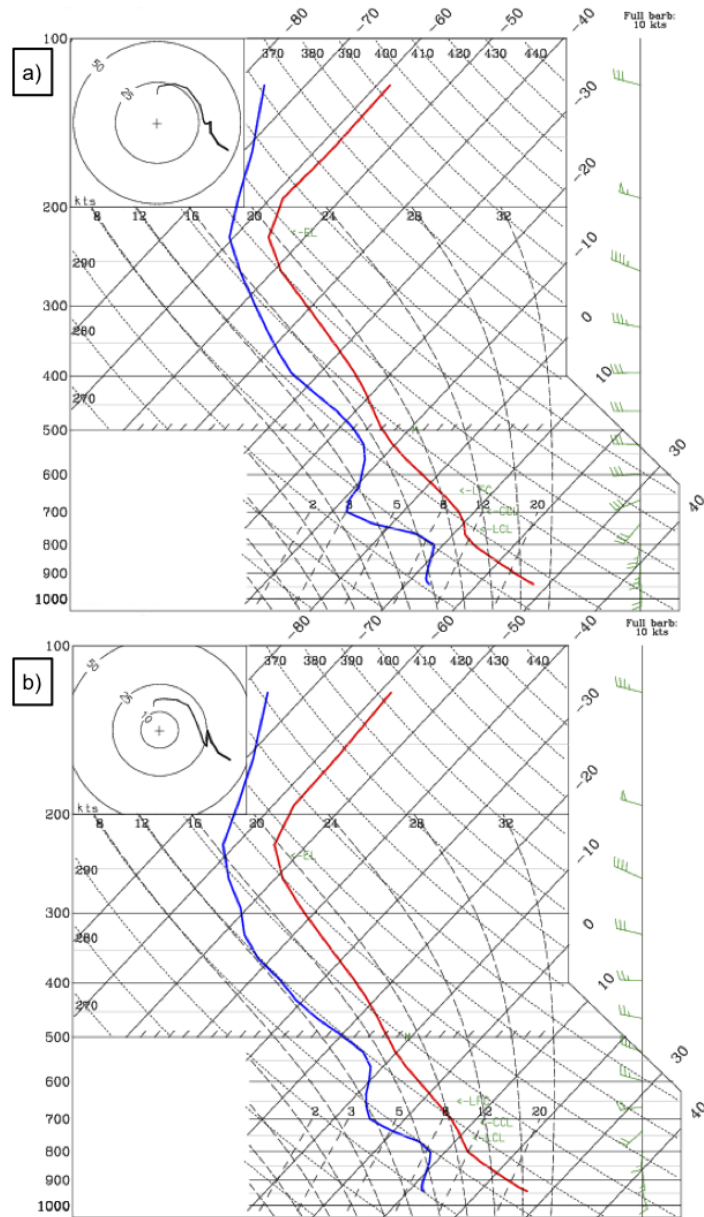


Figure 4.7. (a) good and (b) poor ensemble member average soundings for 2100 UTC 9 Jun at black star location in Figure 4.6.

depicted in Figure 4.9 altering surface and mid-level flow characteristics. The dryline for the good members is approximately 100 km farther east compared with the poor members whose dryline stays situated over western Nebraska. The CAPE builds in the west in the poor members, but a lack of convection moving from behind the dryline into the favorable high CAPE environment keeps the southern extent barren of convection.

The CAPE, CIN, low-level shear, CIN, and southerly LLJ had the large overall environmental differences between good and poor members and is conjectured to have had the largest effect on

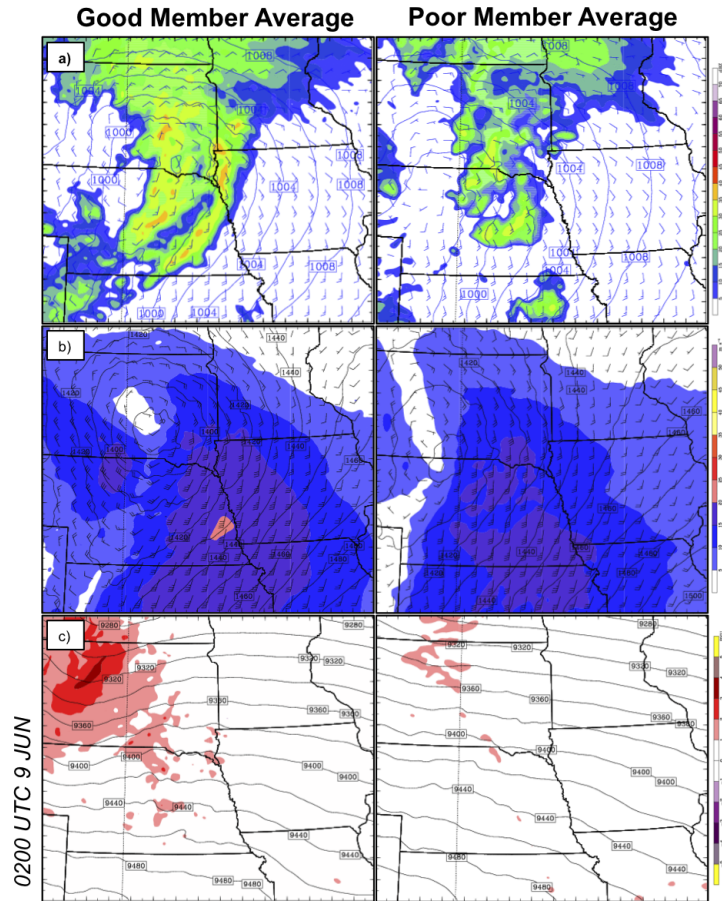


Figure 4.8. Average environment for good and poor members at 0200 UTC 9 Jun indicating (a) simulated composite reflectivity (dBZ), surface winds ($\text{m}\cdot\text{s}^{-1}$), and sea level pressure (hPa); (b) 850-hPa winds ($\text{m}\cdot\text{s}^{-1}$), heights (m), and wind speed (shaded, $\text{m}\cdot\text{s}^{-1}$); (c) 300-hPa PV (shaded every 1 PVU) and heights (m).

the initial evolution of the storms. The star in both maps indicates the initiation point of the primary storms. The good members initiated in a more favorable environment with most unstable CAPE values $>1000 \text{ J}\cdot\text{kg}^{-1}$, less CIN to the east and a stronger southerly flow ($\approx 25 \text{ m}\cdot\text{s}^{-1}$) intersecting the convection. As these storms evolved and propagated east, it is conjectured that more available energy and stronger low-level shear allowed for stronger cold pool development and organization. The southern flow and stronger low-level shear caused a squall line to develop and progress south of the warm front consuming large values of CAPE and intensifying along the southern flank. The poor members initiated convection in lower CAPE values ($<1000 \text{ J}\cdot\text{kg}^{-1}$) with larger CIN to the east and a weaker southerly jet. The larger low-level shear values were 100 km east, unlike the good members that initiated within the strong shear. It is postulated with the lower CAPE, larger CIN, and weaker low-level inflow and shear, the storms took on a multi-cell structure during the initial development phase and propagated more easterly. The low-level shear and CAPE most likely did not support strong cold pools and subsequent squall

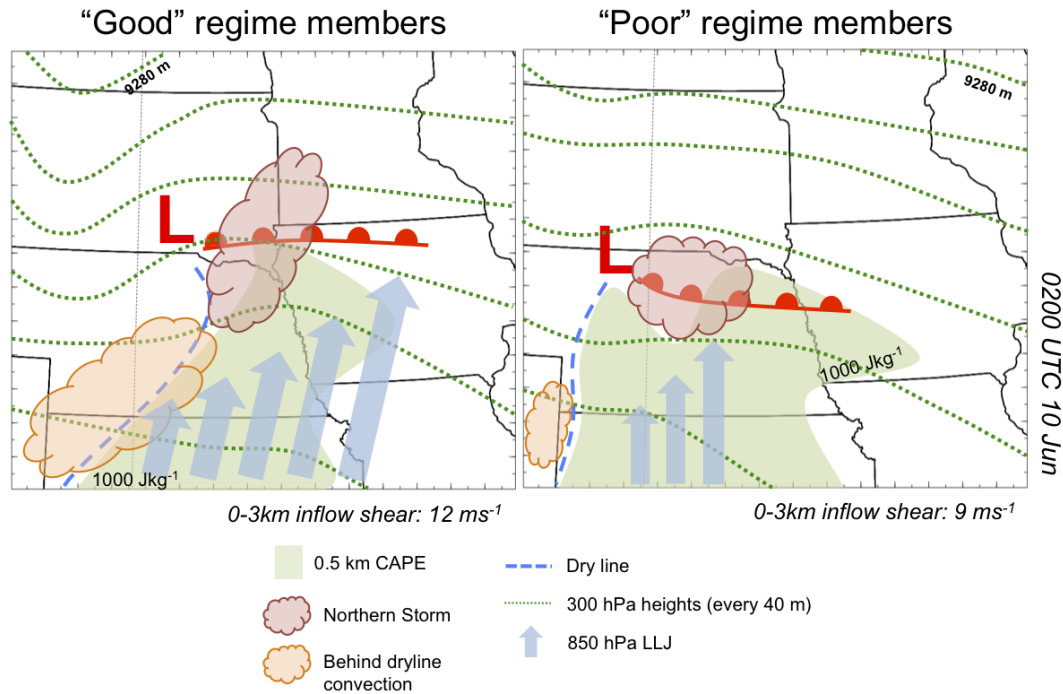


Figure 4.9. Schematic of environment and storm evolution for the good and poor members at 0200 UTC 10 Jun 2003.

line formation. Future work needs to be performed on the effects of low- and mid-level moisture and its impact on the cold pool formation and strength to supplement the current analysis on the squall line and bow echo formation.

4.2 Ensemble Member Cross-Section and Viability

With the model capable of producing bowing features in various members, it is interesting to note the dynamics captured within these members. Figure 4.10.b displays a cross section through the southern bowing segment of ensemble member EN16 (best embodiment of squall line/bow echo features produced by the model for good members) at 0600 UTC 10 Jun, the peak of its storm development. Simulated reflectivity (shaded every 5 dBZ) indicates a clear squall line structure with a high reflectivity core, trailing precipitation region, and a line leading anvil[8]. Storm-relative winds indicate a rear-inflow jet from the rear midlevel down to the leading edge of the convective line and an accompanying surface return flow to the rear. The surface return flow is quite large and is a point of further research although quad-Doppler wind observations from this case have similar surface flow magnitude. The updraft ahead of the high-reflectivity core is slightly tilted towards the rear with flow extending to the rear as an upper-level rear outflow. Figure 4.10.a displays the plan-view of the bowing structure with the cross section indicated from A-A'. The plan view reflectivity values indicate the bowing structure, and the strong couplet of

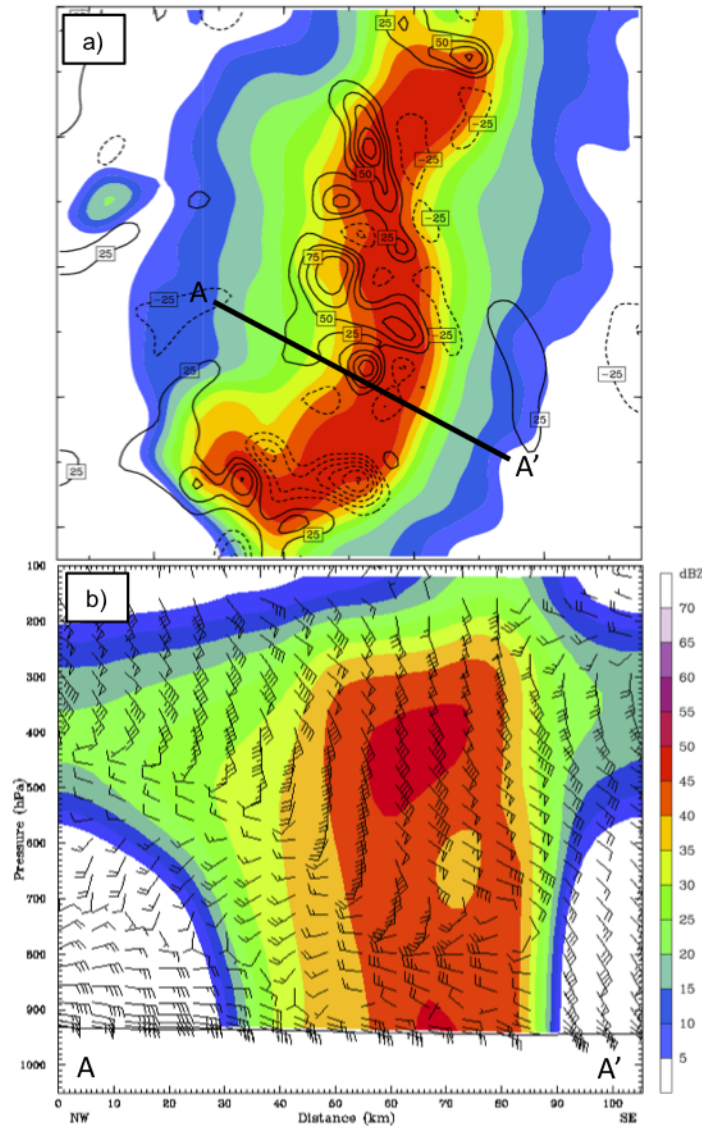


Figure 4.10. Bow analysis for ensemble member EN16 valid 0600 UTC 10 Jun 2003 (a) zoomed in bow region with maximum simulated reflectivity (shaded every 5 dBz) and 3 km relative vorticity (contoured every $25 \times 10^{-5} \text{ s}^{-1}$; dash = negative) (b) cross section with maximum simulated reflectivity (shaded every 5 dBz) and cross section tangent storm relative winds (full barb 5 m s^{-1}). Line A-A' in (a) denotes cross section in (b).

relative vorticity straddling the bow axis suggest bookend vortices, a key dynamical element to a bow echo enhancing the damaging surface winds.[2] The high-reflectivity core is farther up in the troposphere than the observed cross section (not shown), but the overall characteristics and structure are that of the observed bow echo. The tilted updraft, rear-inflow jet, and “bookend vortices” suggest that the model can model the dynamics of squall line and bow echo features[9].

4.3 Ensemble Error Growth

The error growth and predictability of the squall line and bow echo can be examined and quantified through the ensemble spread. A commonly used measure of error and predictability in ensembles is the difference total energy (DTE) [17] [14] [19] [20], which is defined as:

$$DTE_n = \frac{1}{2}(U'^2 + V'^2 + kT'^2) \quad (4.1)$$

where n is the index for each ensemble member. The primes denote the difference between each ensemble member and the ensemble average

$$U' = (u_n - u_{avg}) \quad (4.2)$$

$$V' = (v_n - v_{avg}) \quad (4.3)$$

$$T' = (T_n - T_{avg}) \quad (4.4)$$

and the $k = \frac{C_p}{T_r}$ ($C_p = 1004.9 \text{ Jkg}^{-1}\text{K}^{-1}$ and the reference temperature $T_r = 270 \text{ K}$). [17] The horizontal root-mean difference total energy (RMDTE) is then calculated from (4.1) as the average in either the horizontal (summing in the vertical) or vertical (summing in the horizontal, equation not shown) of the DTE of all ensemble members via:

$$RMDTE_{i,j} = \sqrt{\frac{1}{N_e} \sum_{N=1}^{N_e} \frac{1}{k_{max}} \sum_{k=1}^{k_{max}} DTE_{i,j,k,N}} \quad (4.5)$$

where i and j are the horizontal grid point indices, N is the ensemble member index, and k_{max} is the number of levels in the vertical. The initial conditions included mixing ratio and pressure which are not included in this measure, but the spread of u , v , and T have been shown in previous studies to embody the important error growth dynamics [17] [14] [19] [20].

Figure 4.11 gives the vertically averaged RMDTE for D04 every 2 h starting at 2200 UTC Jun 9. The initial field at 1200 UTC Jun 9 and mid interval 1800 UTC Jun 9 field are shown prior to convective initiation for comparison. The initial RMDTE from the EnKF analysis is approximately $2 \text{ m}\cdot\text{s}^{-1}$ throughout most of the model domain in Figure 4.11.a. The ensemble spread remains steady from initial values through 1800 UTC Jun 9, when the shortwave and associated surface low and trough drive differences in the western portion of the domain. The most significant spread occurs at the onset of convection in central Nebraska at approximately 2100 UTC 9 Jun where values jump to nearly $5 \text{ m}\cdot\text{s}^{-1}$ in the area of convective initiation. This spread continues to increase steadily through 1000 UTC Jun 10 to values in excess of $9 \text{ m}\cdot\text{s}^{-1}$. It is interesting to note the squall line can be detected in the error growth plot, especially in the southeastern region of Nebraska by 0600 UTC 10 Jun. The RMDTE coincides very well with the strong difference in storm mode and squall line structure between members in Figure 4.1. The divergence in solutions is evident by 0600 UTC 10 Jun in Figure 4.11.g with the two distinct

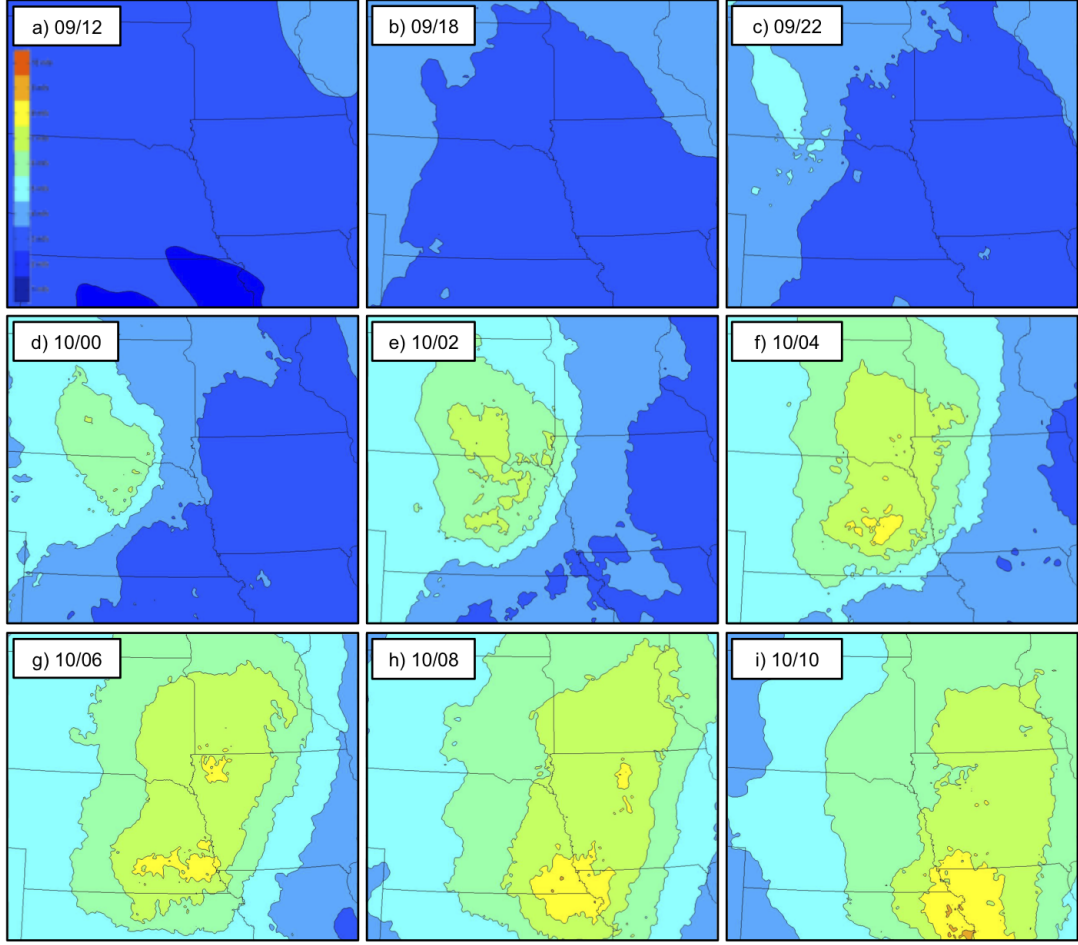


Figure 4.11. Vertically averaged root mean difference total energy between all ensemble members and ensemble member average (shaded every $1 \text{ m}\cdot\text{s}^{-1}$) for (a) 1200 (b) 1800 (c) 2200 UTC 9 Jun 2003 (d) 0000 (e) 0200 (f) 0400 (g) 0600 (h) 0800 (i) 1000 UTC 10 Jun 2003.

areas of large error growth. The largest error growth is in the vicinity of moist convection, which is consistent with Zhang et al. (2003) findings.

The horizontally averaged RMDTE, which is a variation of the vertically averaged RMDTE summing to i_{max} and j_{max} in the horizontal instead of k_{max} in the vertical, is shown in Figure 4.12. Vertical profiles every 3 h starting with the initial analysis at 1200 UTC Jun 9 are shown with pre- and post-initiation profiles indicated by a shift from dash to solid red lines. The pattern of the RMDTE is consistent with previous findings[17] [20] indicating convection had a significant impact on the distribution of RMDTE. Between 1200 and 1800 UTC Jun 9, a small jump from $\approx 1.5 - 2.5 \text{ m}\cdot\text{s}^{-1}$ in spread is evident at approximately 2.5 km which is a signal of the moist processes (precipitation) in the northern part of the domain driven by the synoptic destabilization associated with the shortwave. The large jump at 1.5 km from 2100 UTC 9 Jun to 0000 UTC 10 Jun ($\approx 2.5 - 4 \text{ m}\cdot\text{s}^{-1}$) signifies the beginning of strong convection with a subsequent increase to $\approx 6 \text{ m}\cdot\text{s}^{-1}$ by 0600 UTC 10 Jun indicative of strong error growth associated with moist processes.

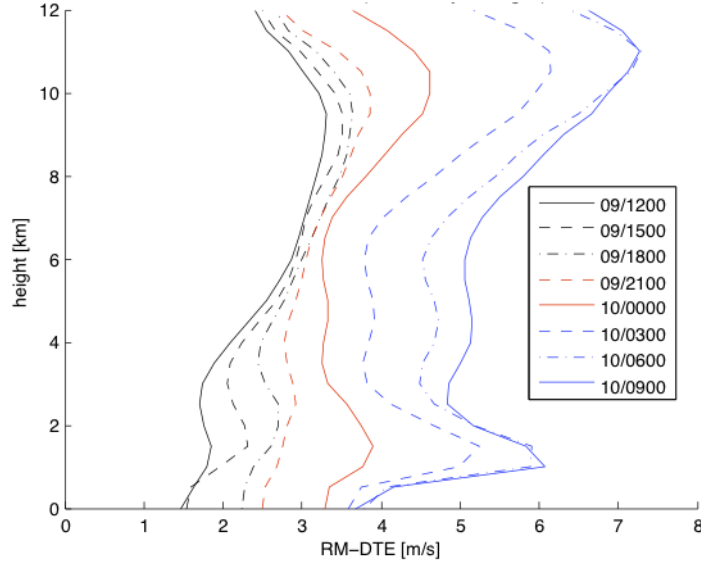


Figure 4.12. Horizontally averaged root mean difference total energy between all ensemble members and ensemble member average shown every 3 h from 1200 UTC 09 Jun 2003 to 0900 UTC 10 Jun 2003.

The peak is located at the same level as previous studies[20] [17] and is where the largest error in temperature and horizontal winds occur associated with convection for this model. The large peak in the upper troposphere centered around 10 km with its increase to $\approx 7.5 \text{ m}\cdot\text{s}^{-1}$ by 0900 UTC Jun 10 is thought to be associated with the upper-level shortwave trough as it progresses through the domain with the strength and temporal difference of the troughs between members causing the large spread.

The DTE analyses in Figure 4.11 and Figure 4.12 show the upscale growth of error due to moist processes that stem from smaller differences in the initial conditions coinciding with previous studies[5] [20] [21]. The exact cause of the divergence between the squall line versus MCS mode cannot be deduced from this measure, but clearly can be seen in the ensemble error growth. A more in depth look at the point of divergence is presented in the following chapters. This chapter drives home the point that deterministic convective numerical weather prediction forecasts are not here, at least for this case, evident by the large variability in the ensemble with extremely small initial condition spread (the most accurate guess currently available). The practical predictability limit has possibly been reached for this case and this method of ensemble initialization.

Chapter 5

Ensemble Categorization and Basic Parameter Analysis

5.1 Categorization of ensemble and subjective ranking

Due to the variability in the ensemble members and the differing storm modes, a method of categorizing the members into similar regimes was developed. This procedure was described previously in Chapter 4 and the resulting groupings are analyzed within this chapter to find any relationship that may exist between the environment and final storm mode and strength.

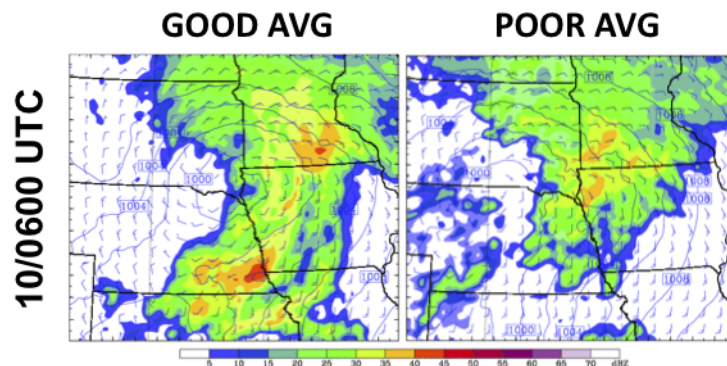


Figure 5.1. Simulated ensemble average maximum reflectivity (shaded every 5 dBz), sea level pressure (hPa), and horizontal wind (full barb $5 \text{ m}\cdot\text{s}^{-1}$) for the subjectively defined good and poor ensemble sets at 0600 UTC 10 Jun 2003.

Plotting and analyzing an average of various data fields for these subjective groupings gives an overall picture of similarities in the members and clear differences between the good and poor regimes. Specifically looking at the simulated reflectivity field (Figure 5.1), a strong reflectivity signal of a squall line stands out in the good members. The reflectivity pattern for the good average in Figure 5.1 looks very similar to the RMDTE pattern in Figure 4.11 at 0600 UTC 10

Jun, in good agreement with the assertion that moist convection of the squall line to the south drives the large error growth.

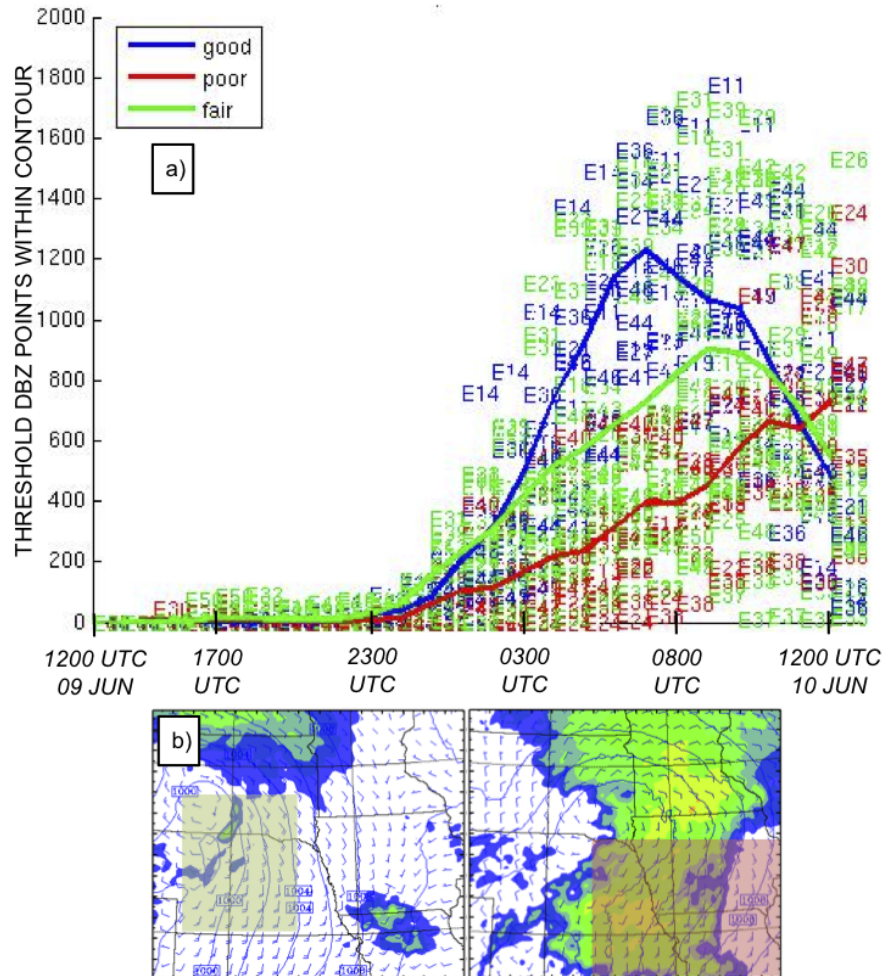


Figure 5.2. (a) number of threshold (45 dBz) grid points falling within the red box of (b) inside the 20 dBz ensemble mean contour for each ensemble member at each time with averages of the subjective sets indicated by colored lines (b) initial and final grid boxes used in DO4 with ensemble average maximum reflectivity (shaded every 5 dBz), sea level pressure (hPa), and horizontal wind (full barb $\text{m}\cdot\text{s}^{-1}$) used for average correlations and determining strength metric used in part (a).

With ensemble members categorized into the good and poor regimes, a strength metric to determine final storm intensity and spatial coverage in comparison to observation is imperative for quantitative comparison. This measure allows correlation analysis between members and parameters affecting storm mode and evolution. To deduce a storm metric, the simulated reflectivity and cold pool with accompanying threshold spatial extent (number of grid points with a specified value) were examined. The cold pool average and minimum surface grid point temperature located below a maximum simulated reflectivity threshold of 45 dBz was compared with environmental ahead of the advancing cold pool computed for each ensemble member at each

time (if high enough reflectivity values were present). These results showed a trend in time with an increase in cold pool strength (lower temperature), coinciding with intensifying simulated reflectivity intensity and coverage. The diurnal effect on the environmental temperature caused a decrease in environmental temperature throughout the storm evolution causing a false trend in the correlation. This led to the abandonment of the cold pool as a solid metric since diurnal affects were having a strong influence on the value.

Trying to quantify strength by composite simulated reflectivity was analyzed because this was the main parameter used in the subjective analysis. A box in the southeastern corner of D04 was examined over the convective activity of interest. The maximum reflectivity and number of points registering a threshold reflectivity of 45 dBz falling within the average simulated 20 dBz reflectivity contour of all ensemble members was documented at each time after convective initiation. Figure 5.2.a shows a temporal evolution with good, fair, and poor averages plotted with associated color-coded members. Also, the domain used for averaging is indicated by the red box in Figure 5.2.b. This metric shows a strong delineation between the designated members and provides a clear, numerical quantity to aide in correlation analysis. Looking at initial parameters and finding statistical correlations to a final storm strength metric has been shown to work in previous studies[20] [27]. These studies had the luxury of a clear cut strength metric such as tropical cyclone central pressure or MCV PV anomaly, but the nature of squall lines and bow echoes convective make quantifying storm strength non-trivial. Other strength metrics such as 700 hPa omega were briefly analyzed, but because of a lack of quantifying the overall spatial coverage due large differences in updraft and downdraft location between members, these were also abandoned. Using the composite simulated reflectivity as the strength metric defined in the previous section (dBZ within a certain contour in the final storm region) provides a general guideline and a better overall judgement of both intensity and spatial coverage. This metric can only be compared within this ensemble and similar model runs due to the variability between different microphysics schemes between different models. The simulated reflectivity was chosen to be the best strength metric for this case and used to determine if any statistical relationship exists.

5.2 Basic correlation and parameter analysis

Correlation does not imply causation, but a statistical trend can indicate a statistical association. The trends between initial severe weather parameters CAPE, CIN, and 0-3 km bulk shear along with average surface temperature, average dewpoint temperature and dBz were analyzed for a statistical significance. An initial area covering the convective initiation region was chosen and the parameters averaged within this region. This value was then compared to the final dBZ strength metric (number of dBZ points and intensity) in the final storm region (both initial and final areas of focus are indicated in Figure 5.2.b). A comparison between initial values within an averaged region at 1200 UTC 9 Jun and following times until convection initiated at 2100 UTC 10 Jun showed no clear trend. This lack of correlation existed between the initial values and storm

strength metric for every ensemble member. This suggests that averaged point correlations are not useful for this case due to the error growth between members associated with convection. The temporal and spatial evolution of these parameters need to be analyzed.

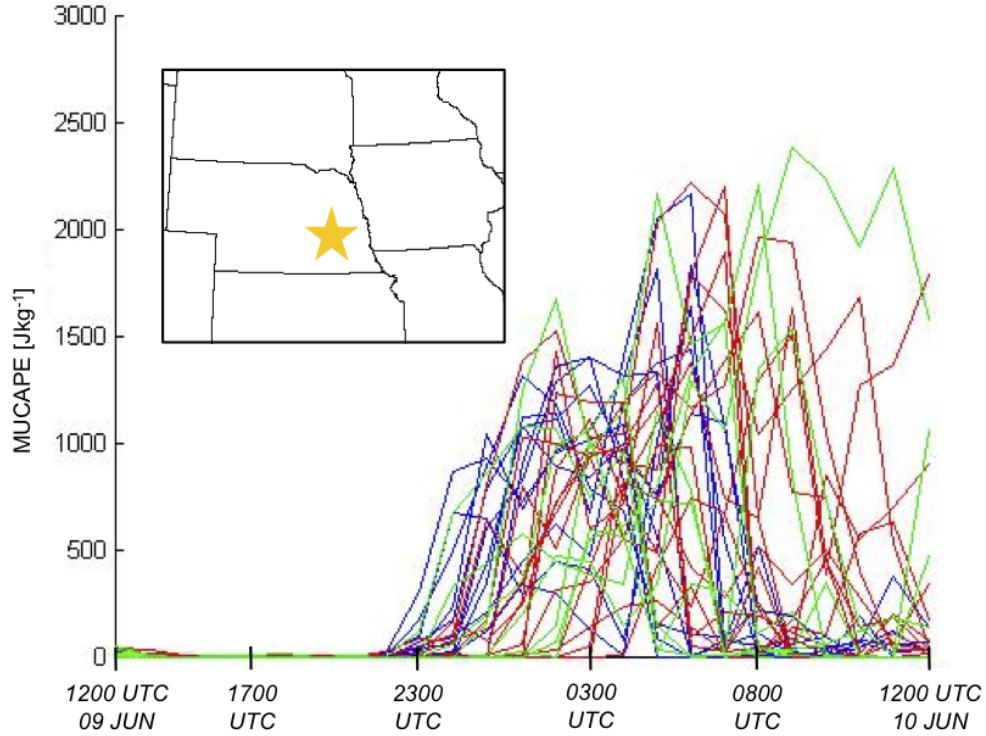


Figure 5.3. Most unstable CAPE versus time for a small averaged point (yellow start designated on D04 map representing the point location - Lincoln, NE) for good (blue), fair (green), and poor (red) ensemble members.

CAPE and low-level shear are shown in previous studies[8] [2] [9] to be a large driving force in squall line and bow echo development and maintenance, and in deducing storm mode. The spatial and temporal evolution of these environmental variables have a large influence on convective initiation and the type of storm that subsequently develops. Analyzing the temporal evolution of the most unstable CAPE, most unstable CIN, bulk shear, surface temperature, and dewpoint temperature at a given point is useful in determining final storm development if convection initiates in the region.

Forecasters often look at point forecast fields to determine the type of storm development. This is done in this study by analyzing the temporal trends of the severe weather parameters. This idea was applied to four locations in D04 that have surface and upper air observations for comparison over the 24-h period for each ensemble member to find a temporal trend in good, fair, and poor members. Figure 5.3 shows the temporal evolution of most unstable CAPE at one of these locations. The temporal evolution shows no apparent difference or trend between the good, fair, or poor ensemble members. The CAPE values increase as expected at the location with the strong southerly jet advecting moisture into Nebraska. Interestingly, the figure shows

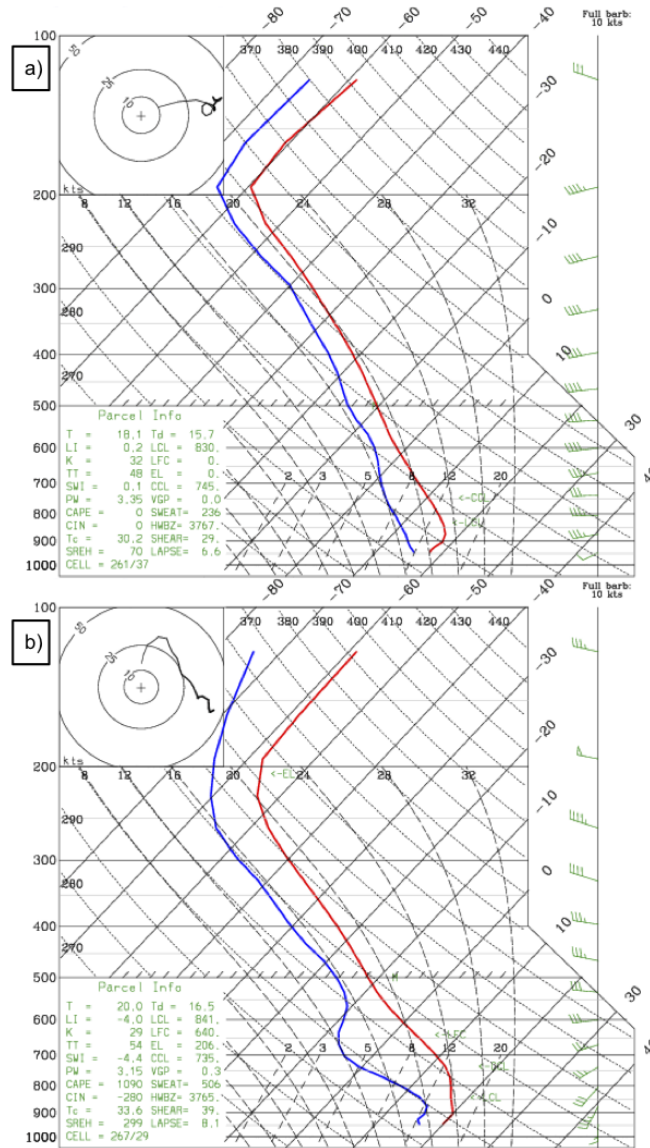


Figure 5.4. (a) good and (b) poor ensemble member average soundings for 0600 UTC 10 Jun at Lincoln, NE (yellow star location in Figure 5.3).

that the all the good members peak and drop back to zero by 0800 UTC 10 Jun, while some fair and good members have lingering higher values which eventually begin to decrease owing to the diurnal cycle. The apparent drop in all good members is thought to be caused by the formation of a squall line that passes over Lincoln NE in all of the good members, resulting in a depletion of the CAPE and dropping the values to zero. Figure 5.4 displays a sounding for both good (Figure 5.4.a) and poor (Figure 5.4.b) ensemble averages at Lincoln, NE (yellow star in Figure 5.3) at 0600 UTC 10 Jun. Differences in CAPE, CIN, shear, and mid-level moisture are evident between the good and poor members resulting from the difference in convection and

its affect on environmental evolution at a single point. The increase and sudden depletion of CAPE around 0500 UTC 10 Jun suggests that the good members evolve and progress similarly by having convection pass over the same region, but does not provide any information regarding why the poor members do not follow this same trend. No comparative trend in the CAPE field was evident for the poor members. The variability in strength and timing of CAPE between the individual members at a single location rule-out using a single point sounding as a predictor for final storm intensity. The noisy signal evident in the CAPE field is indicative of the other parameters analyzed with this method, which helps to reinforce this conclusion.

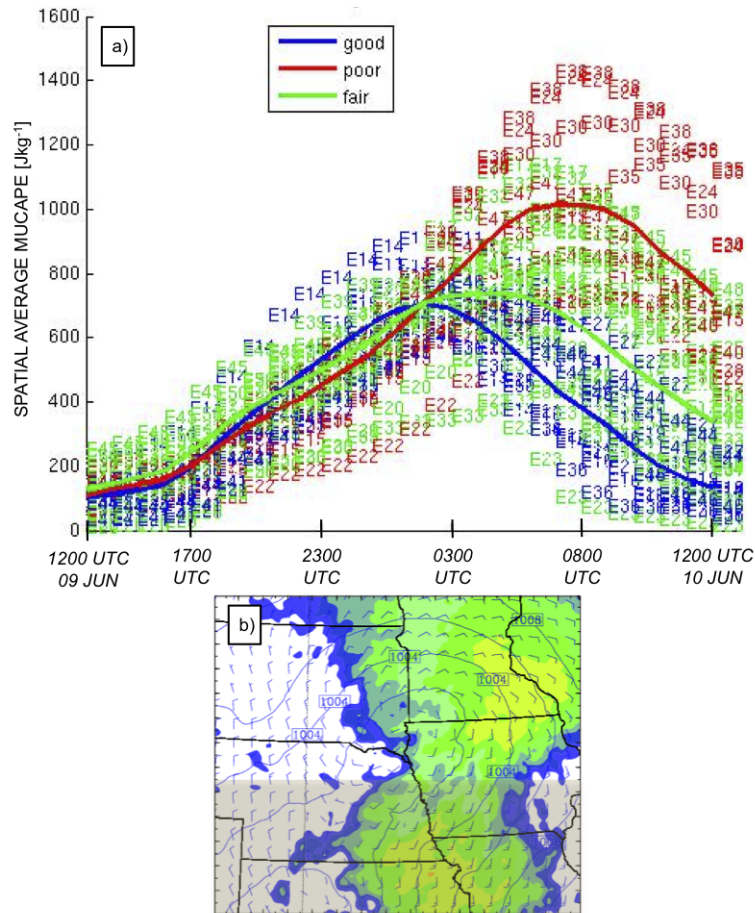


Figure 5.5. (a) spatial average most unstable CAPE for each ensemble member versus time from 1200 UTC 9 Jun to 1200 UTC 10 Jun with averages indicated by the blue (good), green (fair), and red (poor) lines. (b) D04 with gray shaded region used to deduce temporal environmental averages.

Instead of looking at single points in the model that produced noisy signals in the severe weather parameter analysis, the severe weather parameters were averaged over the southern region of D04 to find any average temporal trends between subjective groups environmental fields. Figure 5.5.a shows average most unstable CAPE versus time for the region indicated in Figure 5.5.b. This average reduces the noise in the previous signal and shows a clear pattern. All

of the members start out with similar initial CAPE that steadily increases owing to the southerly advection of moisture and surface heating throughout the region until 1800 UTC 10 Jun. At this time, the good members average becomes $\approx 200 \text{ J}\cdot\text{kg}^{-1}$ higher than the poor members, with the fair members falling in the middle. This difference is driven by the stronger southerly jet of the good members, which is associated with their stronger surface circulation induced by the stronger shortwave aloft. The good members' CAPE values max out around 0200 UTC 10 Jun, when the strong squall line development in these members begin to consume the CAPE. The poor members' CAPE continues increasing until 0800 UTC Jun 10, when the MCS development finally begins to back build far enough into the designated region to alter the average field. The maximum CAPE values and temporal placement are in strong agreement between the members in each subjective group. This agreement and difference in moisture use by the individual storms indicate that a defining point occurs between the good and poor flow regimes that cause the good members to develop southern convection while the poor members do not. Presumably, the good members are able to initiate convection and utilize the moisture field, while the poor members lack a mechanism to trigger convection and utilize the CAPE (this mechanism will be analyzed further in the next chapter).

As mentioned in the previous chapter, the stronger shortwave causes a stronger surface low and stronger cyclonic surface winds. This is clearly evident analyzing the good and poor members, with the good members on average having a ≈ 4 -hPa stronger surface low by 1800 UTC 9 Jun situated over western Nebraska. The surface and 850-hPa wind fields clearly show the stronger southerly winds over central Kansas with associated larger moisture tongues coinciding perfectly with the results shown in Figure 5.5.a. Since the shortwave has a large effect on the evolution of storm parameters prior to convection initiation, the strength of the shortwave was assessed for each member looking at potential vorticity of the 300-hPa trough in D04 as a proxy. Figure 5.6.a shows this analysis of the average PVU within the ensemble average contour within the specified box shown in Figure 5.6.b. Starting after 2200 UTC 9 Jun (the shortwave does not truly progress into D04 until after 1800 UTC, so the values before are not valid for comparison) there is a divergence of the good and poor values, with the good members having ≈ 1 PVU higher potential vorticity from 0000 UTC 10 Jun until the end of the period. Due to the placement of the box, the signal before 2200 UTC 9 Jun is not useful since the trough axis was not within the box region (the larger values for the poor just after 1800 UTC need further study, but the later trend in much larger PVU for the good members is the focus point for this discussion). The higher values of the good members coincide with the observed stronger surface low at later times in the storm development and surface winds altering the moisture inflow into the D04 region later in the storm development (after 0000 UTC 10 Jun). This gives insight into a synoptic effect on the evolution of the environment.

The initial environment (CAPE, 0-3 km shear) over specified regions compared to a final storm strength metric, temporal single point analysis of environmental variables, temporal averaged area analysis of environmental variables, and temporal trough analysis hint at some trends between the good and poor members and storm strength, but lack anything conclusive. The lack of

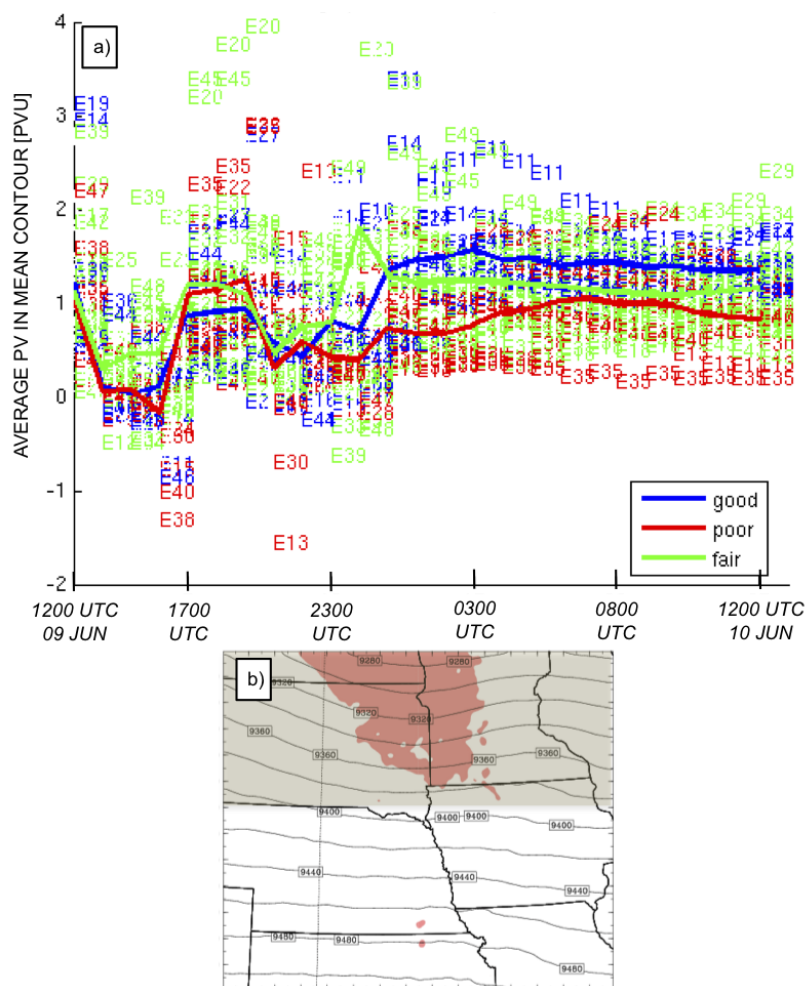


Figure 5.6. (a) average potential vorticity in PVU for each ensemble member within the indicated box and mean contour in (b) versus time with blue (good), green (fair), and red (poor) lines indicating group averages.

predictability in the single point analysis and trends in the averaged area analysis indicate that the single point analysis (i.e. single sounding parameters) is not sufficient in analyzing this event and the spatial and temporal evolution of the environmental variables and their interaction need to be of main focus. The small details on the divergence of the solutions and the effect on predictability cannot be analyzed with the previously defined methods. In order to focus on the forecast divergence of the two distinct regimes, a more effective method needs to be found to focus on the initial spread and subsequent error growth resulting in the divergence in storm mode and intensity. To do this a representative forecast for the good and poor subjective group needs to be specified that embodies the good and poor flow regime and storm mode evolution.

Chapter 6

Ensemble Spread and Predictability

6.1 Experimental setup

With the practical predictability analyzed and storm scale dynamics indicating two distinct storm modes, the intrinsic predictability of the case is examined and explored deeper in this chapter. The intrinsic predictability is the “extent to which prediction is possible if an optimum procedure is used” [13]. To analyze the intrinsic predictability, the initial conditions of the two storm environments subjectively deemed good (10 members) and poor (10 member) are averaged. This defines a set of initial conditions that have the characteristics of the good and poor members. Subsequently, the difference between the two is reduced by averaging between the good and poor set to study the storm divergence evident within the larger ensemble. Owing to the extreme variability and difficulty with temporally and spatially quantifying evolution differences between ensemble members, a “best” representation of the good and poor members, one with a squall line and bow echo formation and one without a southern storm component, is derived to simplify the predictability analysis. To do this, the 10 good and 10 poor subjectively ranked EnKF members at 1200 UTC 9 Jun are combined by averaging their initial conditions to create a single good and poor initial condition set named EFIG and EFIP, respectively. These new analyses have slightly smaller initial condition spread compared to the original members owing to the averaging of the 10 subjective members, but the difference between EFIG and EFIP can be thought of as having the same magnitude error as current analysis fields generated by the EnKF system. The EFIG and EFIP experiments are subsequently modeled to check the viability of the initial fields. Both deterministic forecasts performed extremely well, developing storms representative of the members they embodied.

The horizontal DTE field and vertical DTE distribution from 1200 UTC 9 Jun to 1200 UTC 10 Jun are displayed in Figure 6.1 and Figure 6.2, respectively. Comparing these two measures

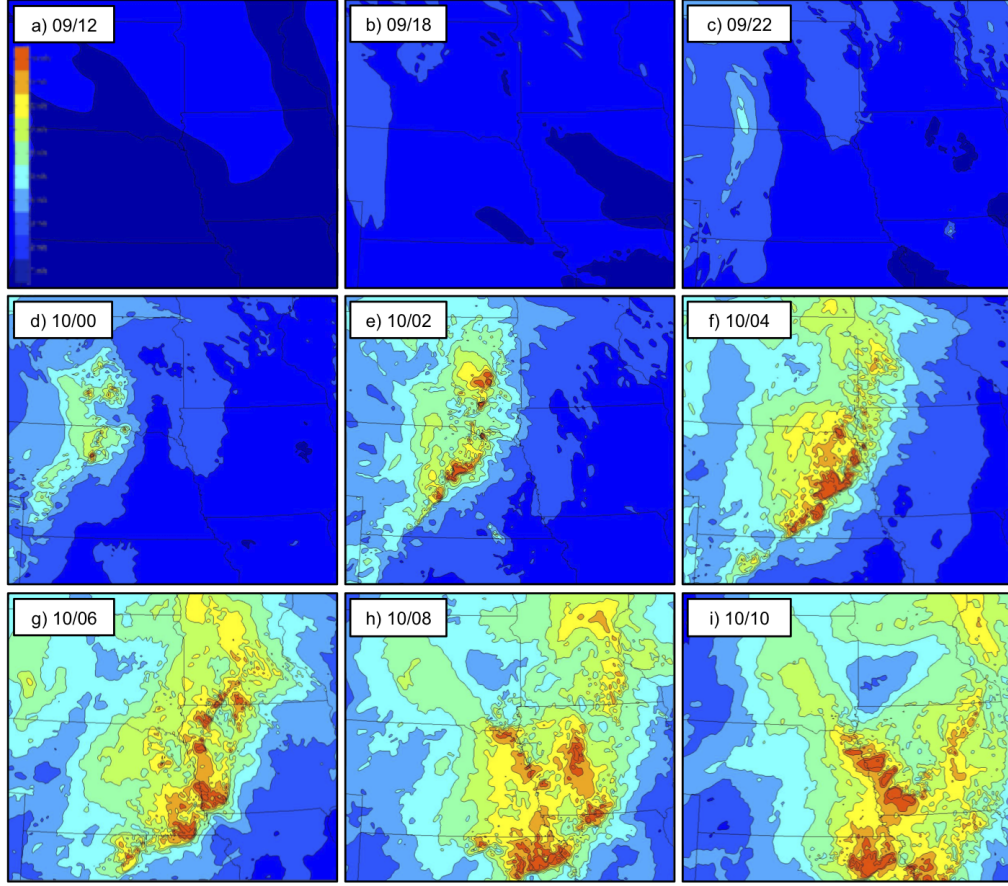


Figure 6.1. Horizontal root mean difference total energy between EFIG, EFIP and ensemble member average shaded (every $1 \text{ m}\cdot\text{s}^{-1}$) for (a) 1200 (b) 1800 (c) 2200 UTC 9 Jun 2003; (d) 0000 (e) 0200 (f) 0400 (g) 0600 (h) 0800 (i) 1000 UTC 10 Jun 2003.

of ensemble spread with that of Figure 4.11 and Figure 4.12, a strong agreement of the error growth of EFIG and EFIP with the error growth of the entire ensemble is evident. The horizontal RMDTE in Figure 6.1 shows a smaller domain average initial error at 1200 UTC 9 Jun, $\approx 1 \text{ m}\cdot\text{s}^{-1}$ compared with Figure 4.11 of the entire 40-member ensemble. The choice of the 10 good and 10 poor have a smaller initial spread than the 40-member ensemble in the analysis error, but by the end of the forecast period they have similar spatial error growth. Figure 6.1 has more noise and detail since it is only two members. The similar evolution of RMDTE reinforces the ability of EFIG and EFIP to embody the entire ensemble and hint at the divergence of certain members. The vertical profile, Figure 6.2, also embodies that of the entire ensemble well and follows all of the same trends in regions of error growth from moist processes and timing associated with strong convective initiation. It is interesting to note even though the initial condition spread for EFIG and EFIP is smaller than the initial ensemble due to the averaging involved in their creation, by 0900 UTC 10 Jun they are almost identical in magnitude due to the upscale error growth associated with moist processes.

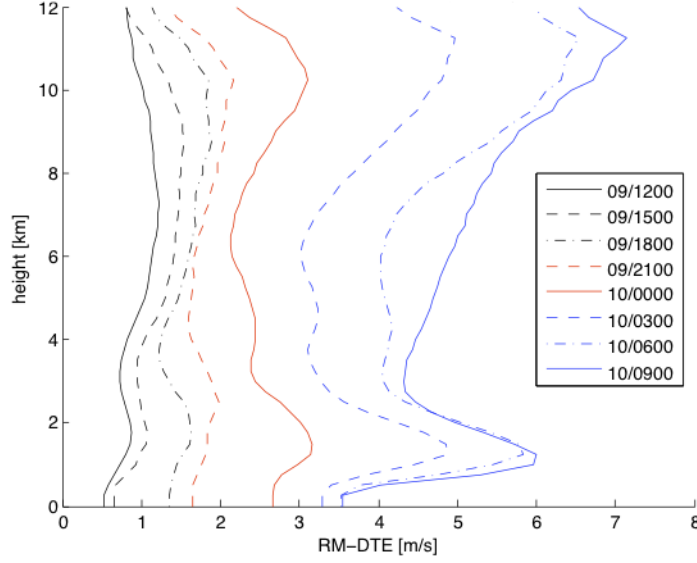


Figure 6.2. Vertical root mean difference total energy between EFIG, EFIP and total ensemble member average shown every 3 h from 1200 UTC 9 Jun to 0900 UTC 10 Jun 2003.

With a baseline set for two ends of the spectrum, the difference between the two members initial conditions was reduced to simulate an improvement in analysis or observations. With this rubric, EFIM is defined as $\frac{1}{2}$ the difference, EFI1 and IFI3 as $\frac{1}{4}$ the difference, and EFIA, EFIB, EFIC, and EFID as $\frac{1}{8}$ the difference. Due to the definition of DTE, the subsequent reduction of initial conditions reduced the initial DTE fields by $\frac{1}{4}$, $\frac{1}{16}$, and $\frac{1}{64}$ the initial difference energy, respectively.

The spectrum analysis of the initial conditions at 1200 UTC 9 Jun in Figure 6.3 indicates consistency among members and clearly shows the decrease in DTE as the initial perturbation is reduced. Figure 6.3 indicates most of the difference total energy between the model runs is concentrated at the larger meso-synoptic scale, wavelengths of 10^3 km and decreases exponentially as the wavelength is reduced to smaller than convective scales (10^1 km).

As the initial condition differences are reduced, the difference total energy between adjacent members (e.g. EFIGEFIM to EFIG-EFIA) is also reduced, indicating the members flow schemes are much closer at every wavelength. When getting down to $\frac{1}{8}$ the initial difference (e.g. EFIG-EFIA), the analysis error between members is extremely small, unattainable by current standards. This unrealistic reduction in initial condition errors is critical in deducing the intrinsic predictability and the exact divergence between the two distinct flow schemes (good and poor members). In between EFIG and EFIP forecasts, a mechanism is responsible for causing the divergence into two separate developing and non-developing squall lines.

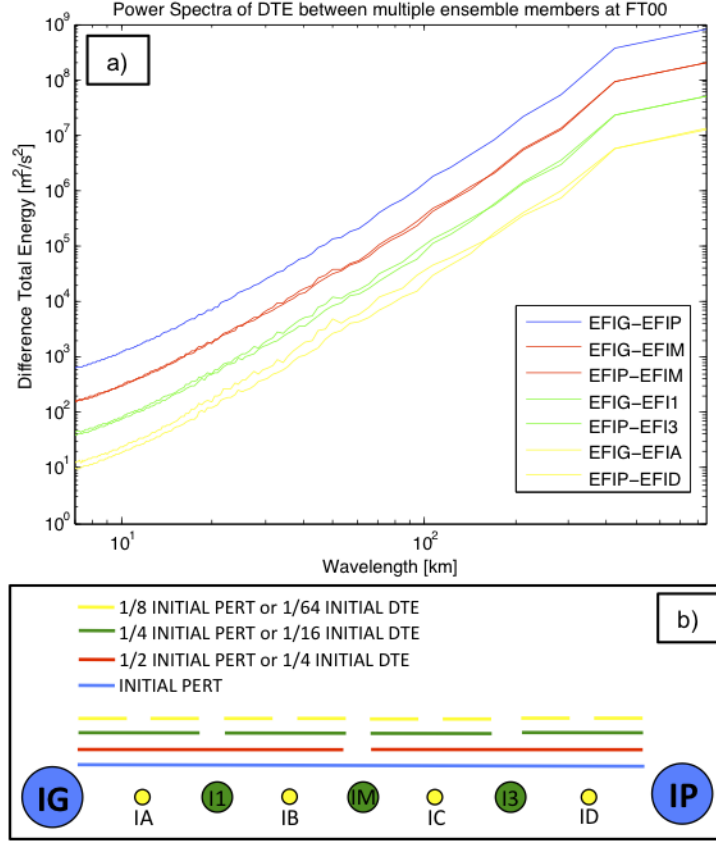


Figure 6.3. (a) power spectra of difference total energy between averaged initial perturbation deterministic forecasts at 1200 UTC 9 Jun; (b) diagram of initial perturbation and difference total energy magnitude for the averaged deterministic forecasts.

6.2 EFIG to EFIP variability

The 7 reduced initial condition members along with EFIG and EFIP are run for 24 h from 1200 UTC Jun 9 to 1200 UTC Jun 10 using identical methods as the 40-members in the previous sections (refer to Chapter 3 for more detail). Figure 6.4 tiles the simulated reflectivity for the 9 forecasts at 0400 UTC and clearly shows the variability. There is a trend toward decreasing squall line formation in the southern portion of the domain from EFIG to EFIP. The variability produced by the reduced initial perturbation forecasts does a good job representing the initial ensemble. Analyzing the evolution of each forecast, a divergence between EFIM and EFIC is clearly seen. The extremely small difference in the initial fields are manifesting themselves as a southern squall line in EFIM and no southern squall line in EFIC. This was deduced subjectively as a bifurcation point, or the dividing line between the EFIG and EFIP flow schemes, indicated in Figure 6.4 by the red line. The surrounding forecasts, namely EFIB and EFI3, are in agreement with the evolution difference. Figure 6.6 illustrates the temporal change of the bifurcating members starting at 0000 UTC 10 Jun after northern convective initiation and proceeding until 0300 UTC

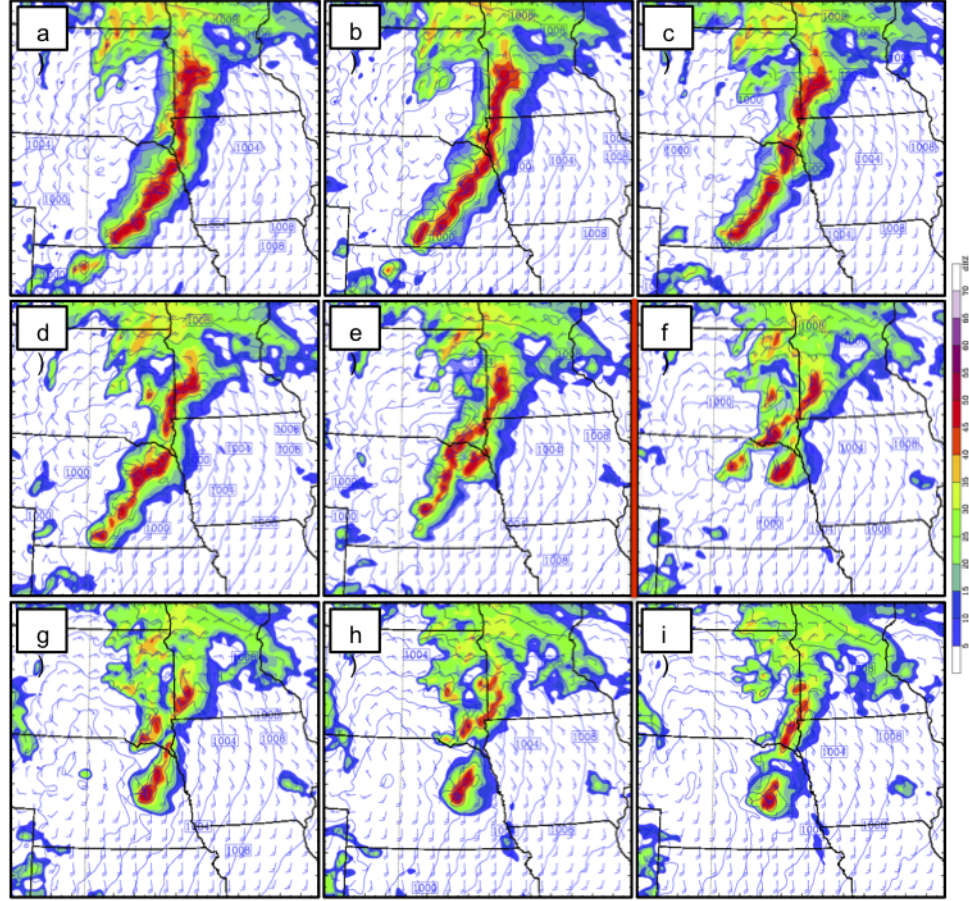


Figure 6.4. Simulated radar reflectivity (shaded every 5dBz), sea level pressure (hPa), and surface winds (full barb $5 \text{ m}\cdot\text{s}^{-1}$) for subjectively defined good and poor averaged initial perturbation deterministic forecasts at 0400 UTC Jun 10. Red line indicates bifurcation point. (a) EF1G (b) EF1A (c) EF1I (d) EF1B (e) EF1M (f) EF1C (g) EF13 (h) EF1D (i) EF1P.

10 Jun where a difference in southern storm mode is evident. Around 0100 UTC, a difference in southern convection (indicated by points A and B on Figure 6.6.a) moving out of northeastern Colorado has a profound impact, driving member EF1C towards a non-developing mode while aiding in the development of the northern squall line. The environments (CAPE, CIN, and 0-3km bulk shear shown in Figure 6.5) of both EF1M and EF1C are almost identical alluding to small-scale error growth modifying the evolution of convection in northeastern Colorado.

6.3 Moist processes error growth: local scale

It has been shown in previous studies[16] [17] [19] [20] that moist convection produces small-scale errors that initially start as sub-convective scale differences and grow upscale to affect larger mesoscale development. The most recent study, Zhang and Sippel 2009, highlighted moist-convection altered cold pool development of a developing tropical depression subsequently di-

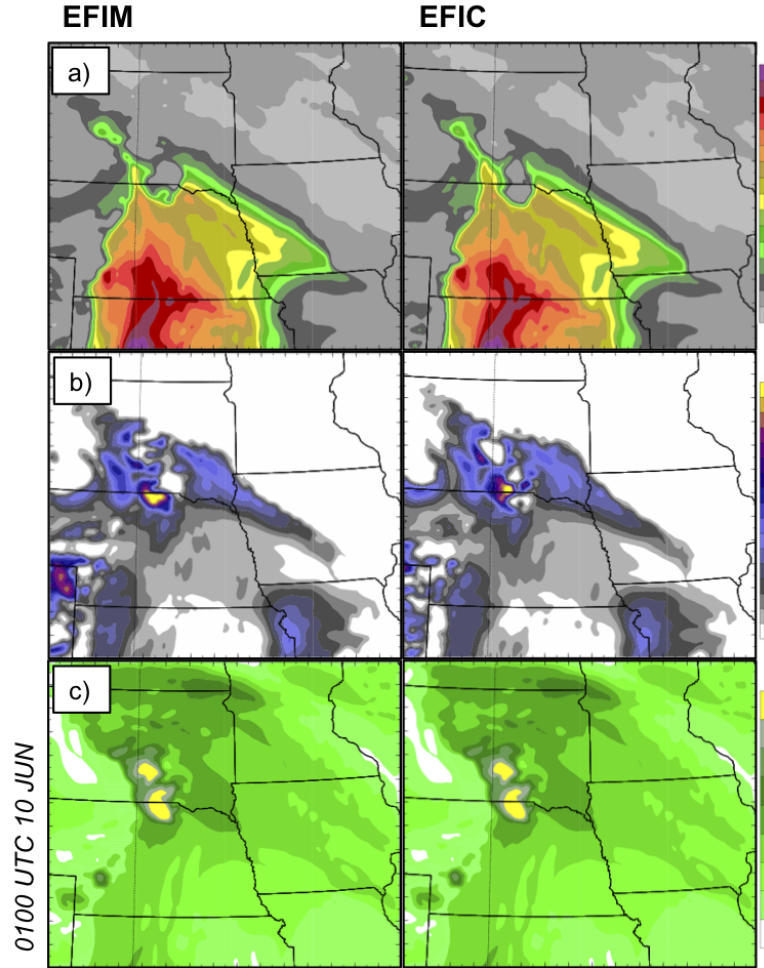


Figure 6.5. (a) CAPE (0.25 km parcel) shaded every $250 \text{ J}\cdot\text{kg}^{-1}$ (b) CIN (0.25 km parcel) shaded every $25 \text{ J}\cdot\text{kg}^{-1}$ and 0-3 km bulk shear shaded every $3 \text{ m}\cdot\text{s}^{-1}$ for members EFIM and EFIC at 0100 UTC 10 JUN.

verging solutions into forming and non-forming hurricanes. The previous study parallels and helps solidify the processes occurring with the convection over northeastern Colorado.

Examining Figure 6.6 more closely, points A and B indicate a clear temporal change between the simulated reflectivity, and hence convective strength, from 0100 UTC 9 Jun to 0200 UTC 10 Jun. Member EFIM has a larger coverage of slightly larger reflectivity at 0100 UTC in central Nebraska that evolves into high reflectivity ($> 40 \text{ dBz}$) returns by 0200 UTC. This same pattern is not evident at point B in member EFIC with weaker reflectivity at 0100 UTC and diminishing returns by 0200 UTC. An initiation threshold has been reached by member EFIM, triggering and maintaining stronger convection near point A while member EFIC does not reach this threshold at point B and diminishes.

The convection initiation thresholds at localized grid points are related to the stability of the atmosphere or surface lift associated with mesoscale boundaries. If substantial lift is created to

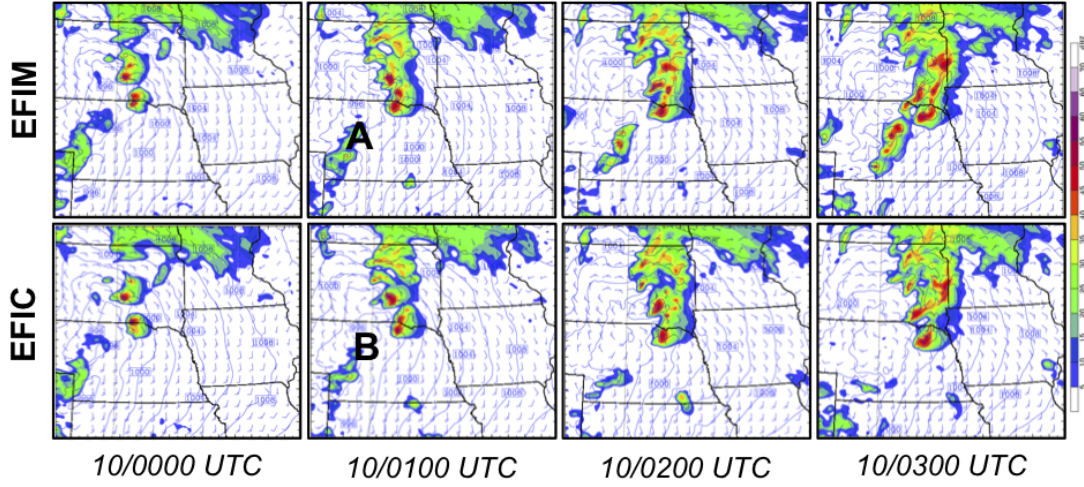


Figure 6.6. Simulated radar reflectivity (shaded every 5 dBz), sea level pressure (hPa), and surface winds (full barb $5 \text{ m}\cdot\text{s}^{-1}$) for EFIM (top) and EFIC (bottom) from 0000 to 0300 UTC Jun 10.

bring a parcel above its LFC, convection will initiate and moist processes will occur. For this case, the surface lift ahead of a cold pool is conjectured to be the threshold criteria driving the difference in convection between members EFIM and EFIC. This threshold can either occur or not occur from the differences in the small-scale details associated with error growth from moist processes. In this case, for the convection evolution differences in northeastern Colorado, it is thought that the difference is driven primarily by cold pool strength differences. This is caused by the small-scale error growth in the microphysics scheme and model that alter the strength and location of the cold pool and the subsequent convergence and lift along the boundary grid points causing small evolution differences to grow upscale through time altering the convective cell timing, location, and strength.

Understanding the local behavior of the cold pools in northeastern Colorado is particularly important for final storm mode. Figure 6.7 indicates the temporal progression of surface virtual potential temperature (Θ_v) and 700-hPa vertical winds (updrafts indicated with solid contours every $1 \text{ m}\cdot\text{s}^{-1}$ and downdrafts indicated with dashed contours every $0.25 \text{ m}\cdot\text{s}^{-1}$). Cold pools are products of convective downdrafts bringing evaporatively cooled air to the surface. The surface Θ_v provides an indicator of cold pool location and strength and 700-hPa vertical velocity indicates convective updrafts and downdrafts. The combination of both properties allows the tracking of individual convective cells and their cold pool evolution and strength.

At 0000 UTC 10 Jun in Figure 6.7, both EFIM and EFIC have convection moving out of northeastern Colorado, but the cold pool associated with EFIM at 0000 UTC 10 Jun is much more pronounced. The error growth due to moist processes cause differences of the convective cell and cold pool locations which cause convergence differences surrounding the cold pools and therefore triggering differences of grid points surrounding each convective cell. These moist processes cause a small-scale divergence of cold pool location and relative strength between member EFIM

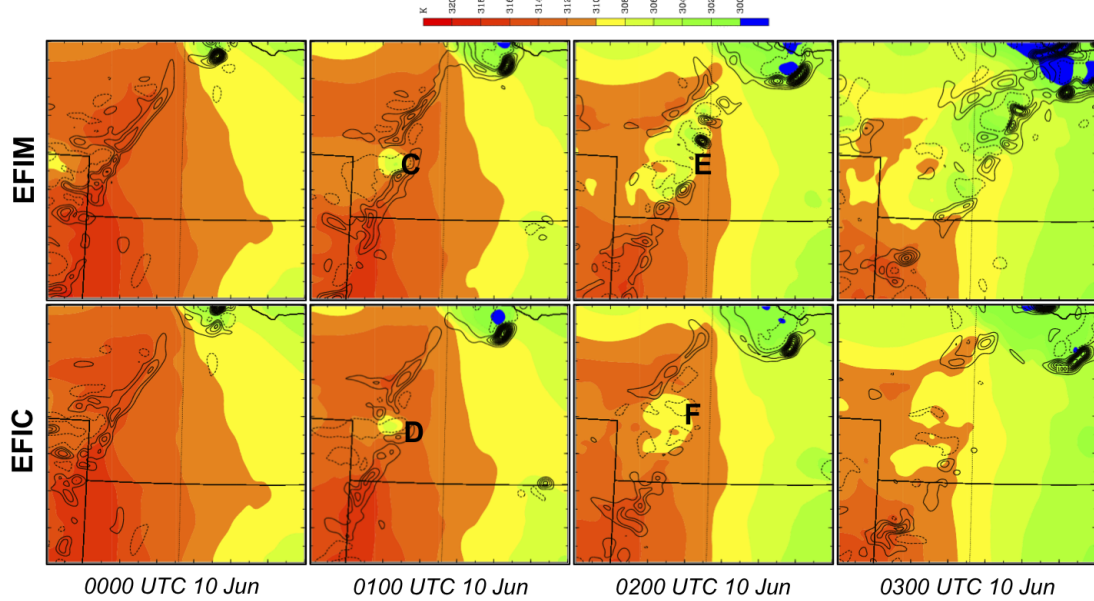


Figure 6.7. Surface virtual potential temperature (shaded every 2 K) and 700-hPa vertical velocity (contoured, solid black contour every $1 \text{ m}\cdot\text{s}^{-1}$ and dashed black every $-0.25 \text{ m}\cdot\text{s}^{-1}$) for EFIM (top) and EFIC (bottom) from 0000 to 0300 UTC Jun 10.

and EFIC, even though environmental conditions are very similar as the convection moves into western Nebraska. This small-scale error growth is the culprit for the difference in evolution of a convective cells indicated at points C and D in Figure 6.7. This cell has propagated to the dry line with the convective cell in EFIM having a larger and relatively colder cold pool indicated by the cooler shading, $\approx 305 \text{ K}$, compared to the weaker, $\approx 307 \text{ K}$, cold pool in EFIC. The vertical velocity is used to determine convective cell strength with stronger updrafts indicating a stronger convective cell. The updraft associated with the weak cell in EFIC at point D is relatively weaker to EFIM and less extensive on its southern edge as it propagates through the dryline. A much broader downdraft is associated with EFIM possibly aiding in the difference in cold pool extent and strength. The cell in EFIM propagates through the dry line and triggers convection on its leading edge in the favorable, high CAPE and low-level shear environment. The convergence at the dry line and strong low level southerly winds on the east side aid in the lift and explosive convective initiation seen from 0100 UTC to 0300 UTC 10 Jun. Point E in Figure 6.7 shows the convective line that developed by 0300 UTC and its associated strong updrafts and downdrafts. The favorable environmental conditions for squall line and bow echo development help evolve the convective line into the later strong southern bow echo. The convective cell in EFIC at the same point does not provide sufficient lift to trigger the strong convective response in the favorable environment evident by the lack of updrafts at point F. By 0300 UTC, the cold pool had dissipated with no convection initiation on its boundaries. The prior moist processes and small-scale errors as convection propagated out of northeastern Colorado led to weaker convection and associated weaker cold pool in EFIC compared with EFIM. This strength difference caused

triggering differences as the cells propagated into the favorable environments with one forming strong convection and filling out the southern line while the other could not trigger convection and ended up dissipating.

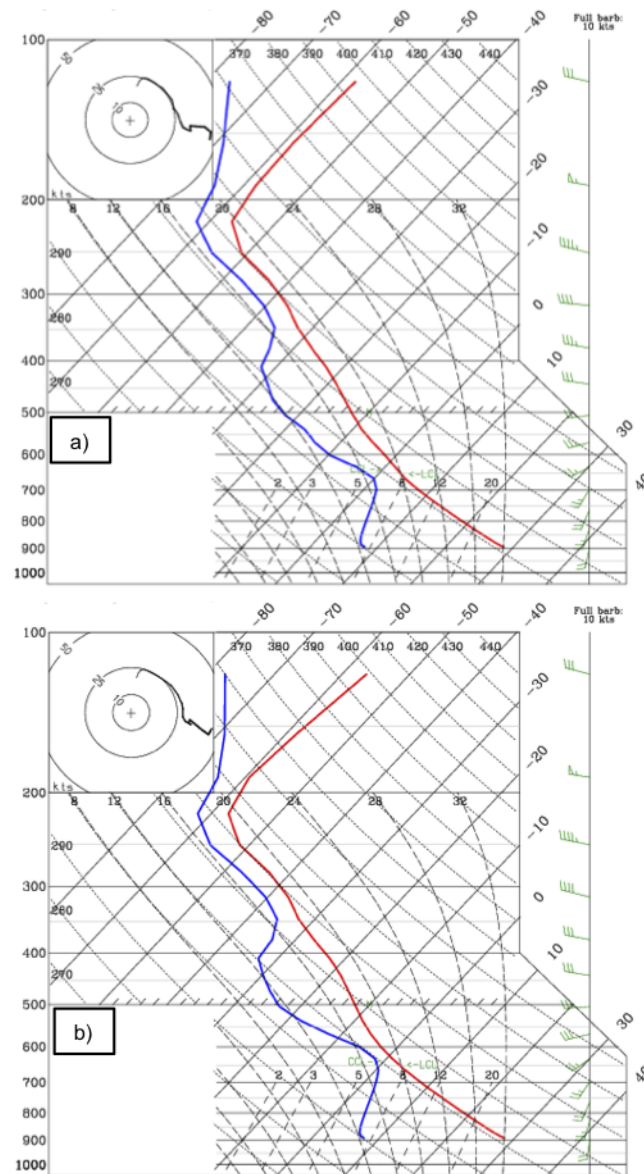


Figure 6.8. Environmental soundings for (a) EFIM and (b) EFIC ahead of the dryline near points C and D at 0100 UTC 10 Jun.

It is important to note that small environmental shear and moisture differences ahead of the dryline may also aid in the triggering difference between EFIM and EFIC by making the environment ahead of the propagating cold pools more conducive for convective initiation. Analyzing the soundings ahead of the dryline for both EFIM and EFIC, Figure 6.8, small differences in the shear and moisture are present. Further study into the affect of these differences on the

convective initiation needs to be performed.

Overall, the small-scale error growth in the microphysics schemes, associated with convection over northeastern Colorado grew upscale causing differences in convective cell strength and spatial location. The spatial extent of one particular cell between two members, EFIC and EFIM, with almost identical environmental conditions pre-dryline, triggered a convective response in EFIM altering the path of the subsequent convection. This divergence of the forecasts marks the bifurcation between the good and poor flow regimes. The strength difference of one convective cell and its effect on model divergence highlights the intrinsic predictability of this case.

6.4 Moist processes error growth: storm scale

The previous section describes the chaotic effect of moist convection on cold pool dynamics, evolution, and subsequent triggering of convection along the dry line by 0200 UTC 10 Jun causing the divergence between EFIM and EFIC. The large-scale flow also has an effect on the development difference between the two distinct storm modes. Figure 6.9 indicates the surface parcel CAPE, CIN, surface divergence, and 0-3 km bulk shear for 2200 UTC 9 Jun, the hour following convection initiation (CI) for members EFIG and EFIP. In both cases, clear environmental differences are seen, primarily in the CAPE and 0-3 km bulk shear. The CIN, caused by an overrunning of warmer lower level air ahead of the low level southerly flow along the weak warm front draped over northeast Nebraska is evident, with CIN values reaching $\approx 125 \text{ J}\cdot\text{kg}^{-1}$ over southwest South Dakota. EFIG and EFIP are very similar in the strength and overall area coverage of CIN, but EFIP has the CIN a little farther to the south. The surface CAPE indicates larger values of CAPE farther north for EFIG, especially in the narrow tongue reaching into central South Dakota. This larger flux of moisture and available convective potential energy, less CIN over northern Nebraska where the storms track, and differences in convective initiation relative to the surface dryline leads to stronger storm development following convective initiation for EFIG. Recalling that EFIG and EFIP are representations of the good and poor flow regimes, it is evident that the two modes have different pre-convective initiation environmental setups derived from the shortwave trough and subsequent surface flow differences. EFIG has a stronger trough, surface low, and subsequent stronger southerly flow advecting moisture farther north. The 0-3km-bulk shear is also slightly stronger over east-central Nebraska, in the path of the northern storm track.

The divergence field seen in the third panel of Figure 6.9 shows similar convergence between EFIG and EFIP along the dry line and warm front intersection, the exact place of convective initiation. Convection initiates around 2100 UTC 9 Jun for both cases, in south central South Dakota, and tracks to the southwest consistent with the direction of 0-6 km mean flow. The larger strength and spatial coverage of CAPE in EFIG along with 0-3 km shear is conducive for strong squall line and bow echo development, especially on the southern flank with a fairly perpendicular intersection of the southerly LLJ. EFIP has a weaker CAPE field with a deficient strip angling southeast through south-central Nebraska. Weaker 0-3 km bulk shear, CAPE, and

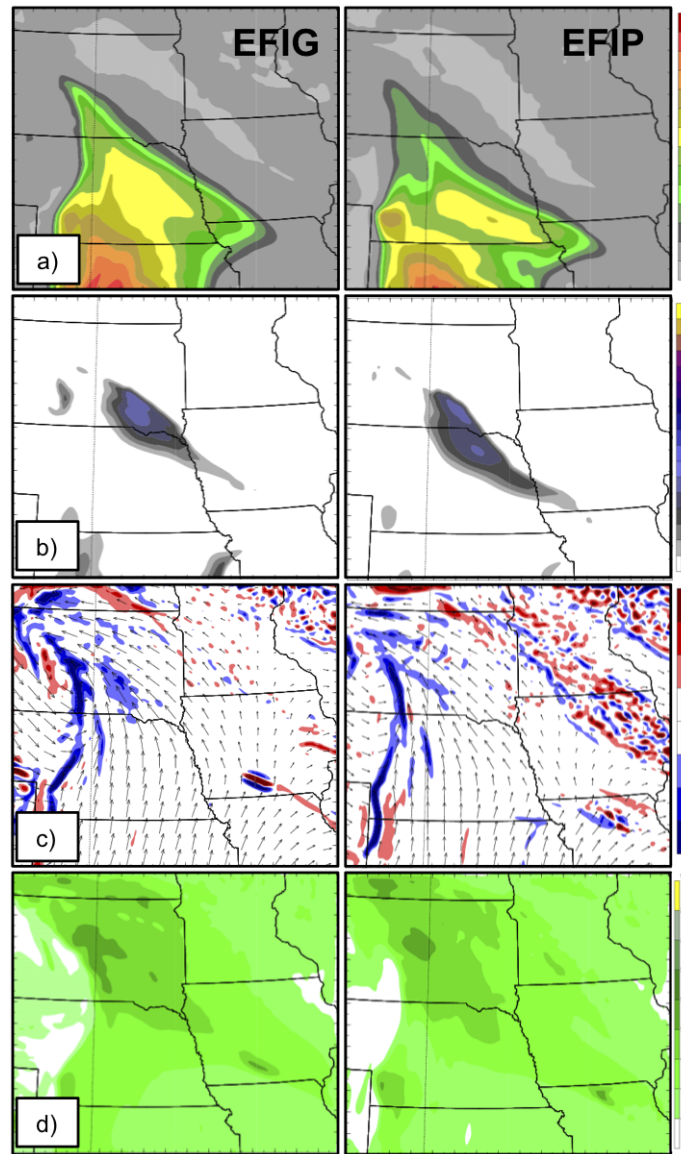


Figure 6.9. (a) surface CAPE shaded every $250 \text{ J}\cdot\text{kg}^{-1}$ (b) surface CIN shaded every $25 \text{ J}\cdot\text{kg}^{-1}$ (c) surface divergence shaded every 1 s^{-1} and (d) 0-3 km bulk shear $\text{m}\cdot\text{s}^{-1}$ for EFIP (left) and EFIP (right) at 2200 UTC 9 Jun.

southerly LLJ lead to a multi-cell storm mode with a more eastward directed track.

Figure 6.10 shows the progression of the CAPE field from 2200 UTC 9 Jun to 0600 UTC 10 Jun clearly indicating the differing storm mode development. Between 2200 and 0200 UTC, the storms in EFIP that develop in the slightly higher 0-3 km bulk shear and moisture rich environment produce stronger and more spatially extensive storms. EFIP develops into distinct, multi-cell storms that travel along the moisture rich environment gradient staying in northeastern Nebraska. Between 0200 and 0600 UTC, the effect of convection in EFIP from northeast Colorado is evident with the explosive and strong convective line, utilizing the CAPE in EFIP as it

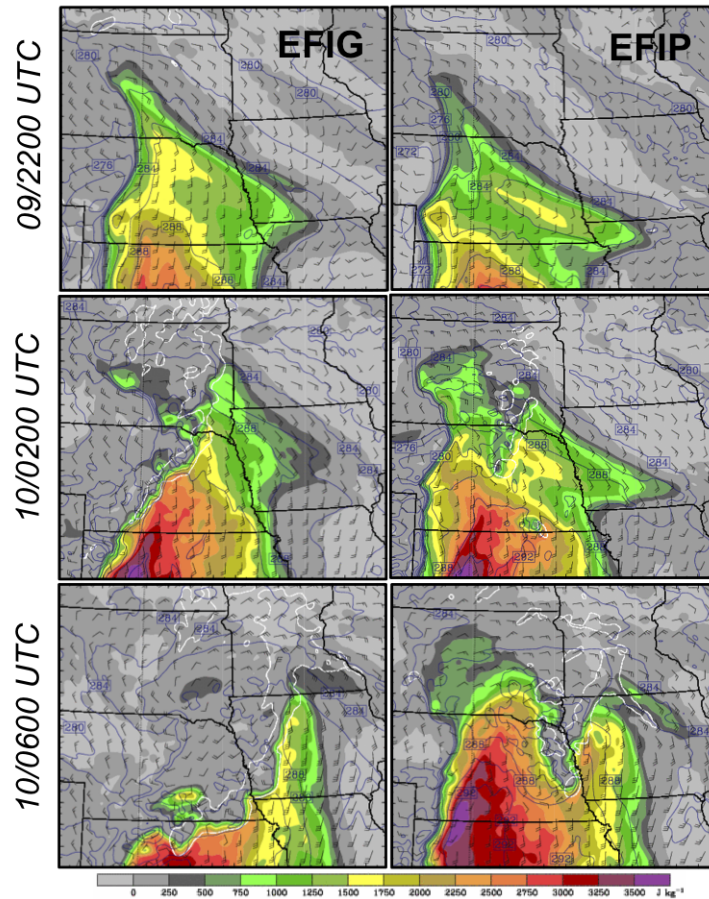


Figure 6.10. Moist unstable CAPE shaded every $250 \text{ J} \cdot \text{kg}^{-1}$, surface dewpoint temperature K (dark blue contour), 0.5 km horizontal winds (full barb is $5 \text{ m} \cdot \text{s}^{-1}$), and 30 dBz simulated reflectivity contoured in white for EFIP (left) and EFIP (right) for 2200 UTC 9 Jun; 0000, 0200 UTC 10 Jun.

progresses through southeastern Nebraska. EFIP does not develop convection to the south and the storms stay to the north, taking on the MCS mode. The CAPE in EFIP drastically builds by 0600 UTC and not utilized since convection was unable to initiate in this region. Even though the environments were similar, small differences in the initial conditions caused temporal evolution differences of the environments allowing for the pooling of CAPE in EFIP over central Nebraska ahead of the dry line that a forecaster would deem “perfect for strong storm development”, but without a triggering mechanism to form convection and utilize the CAPE.

6.5 Intrinsic predictability

The environmental differences evolved from the initial spread in the ensemble lead to evolution differences of the forecasts. Depending where the members lie in relation to the truth and within which flow regime determines the evolution of that member towards the good or poor mode. The top diagram in Figure 6.11 displays a schematic of reducing the initial conditions similar to

the experiment between EFIG and EFIP. The large circle represents the analysis spread of the members of an EnKF analysis with the ensemble average in the center. Two specific flow regimes, good in blue and poor in red, are highlighted to represent the squall line formation and northern MCS formation. The smaller circles represent decreasing the initial spread of the ensemble by decreasing analysis error or observation error. This was performed in the experiment by reducing the initial difference between EFIG and EFIP to EFIM, EFI1, EFIA, and so on.

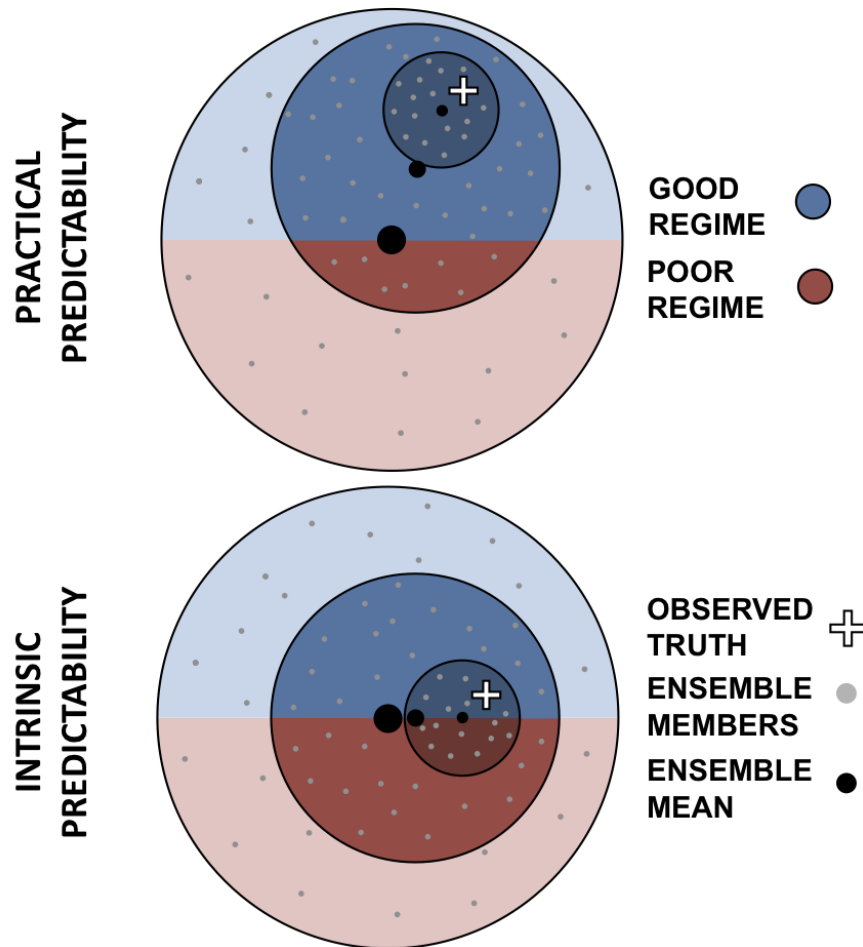


Figure 6.11. Idealized ensemble spread schematic of reducing initial condition error. The top schematic is representative of 9-10 Jun 2003 storm when the observed truth lies predominantly in one flow regime. The bottom schematic highlights a different case when the observed truth lies somewhere close to a divergence point between regimes.

With the current study, the truth lies in the good flow regime, and reducing the initial perturbations within this regime will hone in on the truth and increase the practical predictability of the event. Figure 6.4 clearly displays this trend as the squall line is most representative of the EFIG when the initial condition difference is very small (EFIG to EFIA), both fully lying in the good regime. In other cases, such as environments at the bifurcation point seen in Figure 6.4, when the ensemble circles are moved to encompass a large portion of both regimes, decreasing

the ensemble spread will keep the members lying within both regimes and each ensemble will have members diverging into both regimes. EFIM to EFIC is representative of this case, with the ensemble spread being very small compared to EFIG and EFIP, but EFIM diverges into the good regime while EFIC diverges into the poor regime. Therefore, reducing the initial conditions does not increase the predictability highlighting the intrinsic predictability of the event. Placing the entire ensemble spread in a majority of the poor regime would simulate incorrectly knowing the initial conditions and the observed truth would never be realized, reducing the predictability.

This schematic and application to the current experiment shows the importance of knowing the correct flow regime in relation to the truth and highlights the practical and intrinsic predictability of the forecast. Depending on where the ensemble spread is situated in relation to the truth and regime separation will determine the final evolution of the solution. Better initial conditions with the observed truth more fully in one flow regime will improve practical predictability, but if the observed truth lies close to the bifurcation of the schemes, no amount of improvement will increase the predictability highlighting an intrinsic predictability limit. This is demonstrated in the bottom circle of Figure 6.11.

Figure 6.12 allows for a deeper study and verification of the previous argument looking at the difference total energy between forecasts. Figure 6.12.a displays the difference total energy between the reduced initial condition forecasts over the 24-hour forecast period. At 1200 UTC 9 Jun, the initial error between the members decreases exponentially as the initial difference is decreased, coinciding with the spectral plot in Figure 6.3.a. Comparing the final DTE of each member with the initial field and the difference between subsequent reductions, it can be seen that reducing the initial spread (e.g. EFIG-EFIP) to $\frac{1}{2}$ (e.g. EFIG-EFIM) and $\frac{1}{4}$ (e.g. EFIG-EFI1) does have an effect on increasing the predictability, reducing the final DTE. Noting the difference between the initial and final DTE, it can be seen this relationship is non-linear and each reduction produces a weaker response in final DTE. After reducing the initial spread $\frac{1}{4}$ the original EFIG-EFIA value, no further reduction has any effect on the predictability, except for the extreme EFIG-EFIA and EFIP-EFID cases, which can be thought of as reducing the ensemble spread fully in one flow regime.

The temporal progression indicates an increasing DTE trend until 1000 UTC 10 Jun when all members decrease as convection exits the region. This implies the final useful DTE analysis time is 1000 UTC 10 Jun. The increasing trend in each DTE analysis is driven by the upscale error growth of moist processes and flow differences evolving as information is passed into the domain through the nested boundary conditions. At 1800 UTC Jun 9, a slight divergence occurs between the good (EFIG-EFIM, EFIG-EFI1, etc.) and poor differences (EFIP-EFIM, EFIP-EFI3, etc) caused by convective differences responding to the large-scale shortwave entering the domain.

The DTE drastically increases from 2200 UTC 9 Jun to 0000 UTC 10 Jun in response to convective initiation over south-central South Dakota. The good regime members have a faster increase due to more vigorous convection from stronger forcing and more favorable environmental conditions. The weaker regimes produce less convection, and therefore upscale error growth initially, but chaotic progression in the northern MCS eventually strengthens and surpasses that of

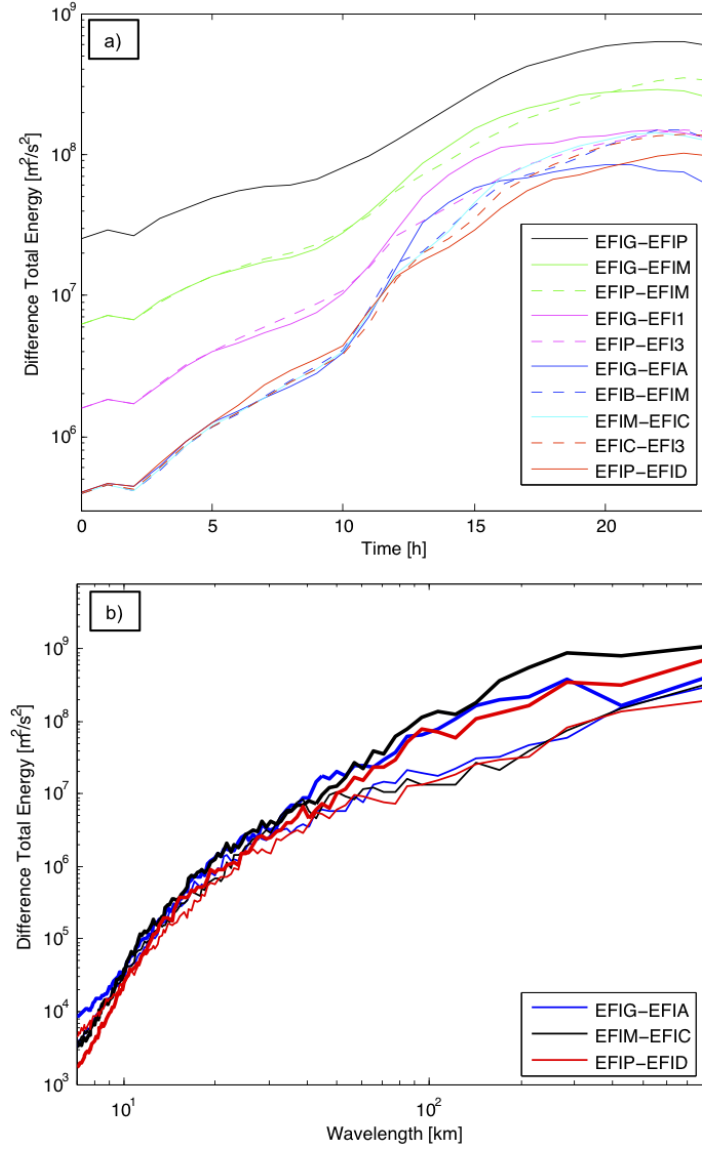


Figure 6.12. (a) The time evolution of domain-integrated difference total energy (DTE) between specified members from 2200 UTC 9 Jun to 1200 UTC 10 Jun; (b) power spectra of DTE between specified members at: thin lines 0000 UTC 10 Jun and thick lines 0900 UTC 10 Jun.

the good regime by 0800 UTC 10 Jun. Comparing the initial condition spread versus final DTE, it is shown the $\frac{1}{4}$ and $\frac{1}{8}$ converge by 1000 UTC 10 Jun, resulting in no gain in predictability by decreasing the initial spread. The two EFIG-EFIA and EFIP-EFID due to their full embodiment in their respective regime, each converge to their respective mode and therefore increase in predictability. If it were somehow possible, correctly identifying the flow regime of the ensemble and decreasing the ensemble spread within the flow regime will allow for an increase in predictability.

Focusing more closely on the bifurcating forecasts, EFIM and EFIC, by 0100 UTC 10 Jun,

the forecasts DTE begin to diverge identically to the EFIG-EFIA and EFIP-EFID response at 2200 UTC 9 Jun. This divergence into each respective regime is evident with the similar trend as the good regime develops a squall line, while the poor regime remains convectively barren to the south. This point indicates roughly the exact time of forecast divergence into the respective regimes and is possibly explained by the cold pool argument of bifurcation.

Figure 6.12.b is a power spectra decomposition of DTE for member EFIG-EFIA, EFIM-EFIC, and EFIP-EFID at 0000 UTC 10 Jun (thin solid line) and 0900 UTC 10 Jun (thick solid line). This plot shows the distribution of DTE at specific wavelengths allowing for the analysis of DTE at each scale. Comparing the overall trend between times, it is evident that the DTE is saturated (cannot get any larger at this specific wavelength) from 10 *km* to 40 *km* covering the small convective scales. Convection initiation at 2100 UTC 9 Jun in all members increases small-scale error and provides upscale error growth associated with moist processes, saturating the small-scales on the $O(1h)$ [17]). The subsequent upscale error growth cascades into the larger scales by 0900 UTC 10 Jun with much larger DTE values (order of magnitude) at wavelengths above 60 *km*. The DTE at 0000 UTC 10 Jun is very similar and in agreement between the forecasts embodying each regime (EFIG-EFIP, EFIP-EFID) and a mix of regimes (EFIM-EFIC). The divergence of the solution has not taken place by this time and upscale growth has yet to drastically affect the larger scales. The DTE by 0900 UTC 10 Jun shows exponential error growth at larger wavelengths indicating the cascade of upscale error growth. EFIG-EFIA and EFIP-EFID being in the same flow regime and smaller errors compared with EFIM-EFIC which embodies both regimes.

The preceding chapter highlights the practical and intrinsic limits of predictability with this case and can be applied more generally to encompass the fundamental concept. Reducing the spread in an ensembles initial conditions will not necessarily increase predictability. It depends on the flow regime and where the truth lies relative to the different flow regimes. Having the truth lie predominantly in one of the regimes will increase the predictability of the event, but if it is near a point encompassing both regimes, decreasing initial conditions will not aid in increasing predictability. Knowing the initial conditions more thoroughly will aid in predictability only if the observed truth lies predominantly in one flow regime. The analysis of the bifurcating member EFIM-EFIC indicate the extreme sensitivity to small-scale error growth by moist processes and the small-scale error growth that grow upscale and lead to regime divergence. The distinct flow regimes place an intrinsic limit of predictability in the EFIM-EFIC case. Small-scale error growth associated with moist processes lead to a divergence between good and poor regimes limiting the predictability.

Chapter 7

Concluding Remarks

7.1 Discussion and Summary

In this study, an ensemble of cloud-resolving Weather Research and Forecasting Model (WRF) forecasts initialized with perturbations from an ensemble Kalman filter (EnKF) analysis is used to explore the predictability of a bow echo event during the Bow Echo and MCV Experiment (BAMEX) on 9-10 June 2003. The success of deterministic WRF model forecasts during BAMEX gave the illusion that convective scale NWP had arrived, but the examination of an ensemble of simulations with realistic initial conditions proved the contrary. The limit of practical predictability for this case may have been attained, shown by the large variability in evolution, mode, and flow regime. Commonly used severe storm predictors based on single soundings (e.g. CAPE, CIN, and low-level shear at a single point in the environment) do not provide a consistent sampling of the environment due to local effects and indicate no correlation between initial parameters of the ensemble members and final storm mode and strength. This suggests the need for both spatial and temporal evolution analysis of these parameters in relation to convective formation and evolution. Subjectively choosing good and poor members defining two distinct regimes allowed for the analysis of initial condition spread on final storm mode. Reducing initial condition uncertainties and performing deterministic forecasts simulating decreased ensemble spread within specific regimes were run to highlight the intrinsic predictability and deduce the bifurcation point of the southern aspect of the squall line development between the good and poor regimes.

The ensemble indicated vast variability with members developing strong squall lines and bow echoes that resembled observations, while others had no southern squall line development maintaining a multi-cell mode in the northern part of the domain. This variability was confirmed with a temporal analysis of Root Mean Difference Total Energy (RMDTE) for the ensemble, with the greatest error growth associated with moist processes in the southern squall line and northern MCS convection. Moist processes dominated the spread, with large increases in vertical RMDTE at 1.5 to 2 km, consistent with previous studies, and located where strong differences

in latent heating are occurring. The realistic initial conditions for the ensemble, produced by the EnKF system, were smaller than FNL-GFS analysis and WRF3DVar analyses run concurrently, indicating the practical predictability inherent in the current initial condition level of accuracy. The divergence of the members into two separate modes indicates the dependence of each ensemble member on the flow regime caused by upscale error growth from moist convection. Given the uncertainty, error growth, and variability in ensemble forecasts, the deterministic convective numerical prediction for this case has yet to be attained.

Trying to predict ensemble member strength and storm mode by commonly used single sounding severe weather parameters proved to be futile, with no correlation between initial fields and final storm strength. The subjective groups showed temporal trends in CAPE, CIN, low-level shear, surface temperature, and surface dewpoint over averaged areas in the southern half of the domain. Convective scale features drove the evolution of the parameters, with spatial and temporal placement of storm cells designating the trends in the parameter fields. An analysis of the potential vorticity allowed for a clear visual difference of the shortwave trough in the northern part of the domain which alluded to the strong difference in final storm outcome dependent on trough axis placement and strength. It was determined that composite simulated reflectivity was the best storm metric for comparison between members and time due to its embodiment of both intensity and storm spatial structure.

Using a perfect model assumption made in conjunction with initial condition uncertainties an order of magnitude smaller than the current observational analysis, the intrinsic predictability of the storm was analyzed. The subjectively averaged 10 good and 10 poor members are linearly reduced by $\frac{1}{2}$, $\frac{1}{4}$, and $\frac{1}{8}$ to produce the initial condition uncertainties. A bifurcation of forecasts could be seen within the linearly reduced forecasts highlighting an intrinsic predictability limit for this case. Simulating reduced ensemble spread lying predominantly in each regime and encompassing both regimes allowed for the study of the bifurcation point between members. The divergence of the solutions was found to be caused by upscale error growth associated with moist convection from upslope over the Cheyenne ridge in northeastern Colorado. The cold pool spatial coverage and strength difference associated with moist processes led to vastly different cold pool evolution that reached the dry line in western Nebraska. The strength of the cold pools in the good regime allowed for the explosive triggering of convection along the dry line providing sufficient surface convergence and lift along its edge, while the poor regime members cold pool did not have the strength to trigger convection on the leading edge. This led to the good regime producing a southern squall line and bow echo and the poor regime leaving the southern domain barren of convection.

This divergence highlights the limit of predictability associated with upscale error growth from moist processes and random triggering caused by cold pool dynamics. If the initial ensemble spread encompasses both regimes with the truth lying within the ensemble spread and close to the divergence point, reducing the initial conditions will provide no improvement in predictability since both solutions will be realized, highlighting an intrinsic limit. Reducing initial conditions when the observed truth is predominantly within one flow regime increases practical predictability

of the event, with the solutions converging to the specific regime truth.

It was seen analyzing the difference total energy (DTE) that reducing the spread in the initial condition does not linearly decrease the final DTE. The response is non-linear and a point is reached where decreasing the initial spread does not improve the predictability of the event, except when the correct flow regime is modeled. There is an intrinsic limit to the predictability of an event based on the regime being forecast and if the observed truth and ensemble spread has a majority of its members in the correct flow regime. Improving initial conditions in a divergent spread when the observed truth is near a bifurcation point may produce an intrinsic limit to predictability.

The ensemble forecast and sensitivity experiments demonstrated that this storm has a practical limit in its predictability given realistic initial condition uncertainty and the predictability can be improved with more accurate and precise initial conditions. If a theoretical storm is near a bifurcation point and improvements are made to the accuracy and precision of the initial conditions, there may be an intrinsic limit to its predictability.

Bibliography

- [1] FUJITA, T. (1978) “DOWNBURSTS AND MICROBURSTS AN AVIATION HAZARD,” *American Meteorological Society*, pp. 102–109.
- [2] WEISMAN, M. (1993) “The genesis of severe, long-lived bow echoes,” *Journal of the Atmospheric Sciences*, **50**(4), pp. 645–670.
- [3] JOHNS, R. and W. HIRT (1987) “Derechos: Widespread convectively induced windstorms,” *Weather and Forecasting*, **2**(1), pp. 32–49.
- [4] JOHNS, R. (1993) “Meteorological conditions associated with bow echo development in convective storms,” *Weather and Forecasting*, **8**(2), pp. 294–299.
- [5] MENG, Z. and F. ZHANG (2008) “Tests of an ensemble Kalman filter for mesoscale and regional-scale data assimilation. Part III: Comparison with 3DVAR in a real-data case study,” *Monthly Weather Review*, **136**(2), pp. 522–540.
- [6] (2010), “AMS Glossary,” This is an electronic document. Date of publication: [Date unavailable]. Date retrieved: March 1, 2010. Date last modified: [Data unavailable]. URL <http://amsglossary.allenpress.com/glossary>
- [7] NOLEN, R. (1959) “A radar pattern associated with tornadoes,” *Bull. Amer. Meteor. Soc.*, **40**, pp. 277–279.
- [8] ROTUNNO, R., J. KLEMP, and M. WEISMAN (1988) “A theory for strong, long-lived squall lines,” *Journal of the Atmospheric Sciences*, **45**(3), pp. 463–485.
- [9] WEISMAN, M. and C. DAVIS (1998) “Mechanisms for the generation of mesoscale vortices within quasi-linear convective systems,” *Journal of the Atmospheric Sciences*, **55**(16), pp. 2603–2622.
- [10] JAMES, R., P. MARKOWSKI, and J. FRITSCH (2006) “Bow echo sensitivity to ambient moisture and cold pool strength,” *Monthly Weather Review*, **134**(3), pp. 950–964.
- [11] DAVIS, C., N. ATKINS, D. BARTELS, L. BOSART, M. CONIGLIO, G. BRYAN, W. COTTON, D. DOWELL, B. JEWETT, R. JOHNS, ET AL. (2004) “The Bow Echo and MCV Experiment,” *Bull. Amer. Meteor. Soc.*, **85**, pp. 1075–1093.
- [12] (2006), “Bow Echo and MCV Experiment (BAMEX),” This is an electronic document. Date of publication: November 2006. Date retrieved: March 1, 2010. Date last modified: [Data unavailable]. URL <http://www.crh.noaa.gov/lxx/science/bamex/bamex.php>
- [13] LORENZ, E. (1969) “Atmospheric predictability as revealed by naturally occurring analogues,” *Journal of the Atmospheric sciences*, **26**(4), pp. 636–646.

- [14] ZHANG, F., A. ODINS, and J. NIELSEN-GAMMON (2006) "Mesoscale predictability of an extreme warm-season precipitation event," *Weather and Forecasting*, **21**(2), pp. 149–166.
- [15] ERRICO, R. and D. BAUMHEFNER (1987) "Predictability experiments using a high-resolution limited-area model," *Monthly Weather Review*, **115**(2), pp. 488–504.
- [16] ZHANG, F., C. SNYDER, and R. ROTUNNO (2002) "Mesoscale predictability of the surprise snowstorm of 24–25 January 2000," *Monthly Weather Review*, **130**(6), pp. 1617–1632.
- [17] ——— (2003) "Effects of moist convection on mesoscale predictability," *Journal of the Atmospheric Sciences*, **60**(9), pp. 1173–1185.
- [18] TAN, Z., F. ZHANG, R. ROTUNNO, and C. SNYDER (2004) "Mesoscale predictability of moist baroclinic waves: Experiments with parameterized convection," *Journal of the Atmospheric Sciences*, **61**(14), pp. 1794–1804.
- [19] ZHANG, N. (2007) "Impacts of initial condition errors on mesoscale predictability of heavy precipitation along the Mei-Yu front of China," *Quarterly journal of the Royal Meteorological Society*, **133**(622 PART A).
- [20] HAWBLITZEL, D., F. ZHANG, Z. MENG, and C. DAVIS (2007) "Probabilistic evaluation of the dynamics and predictability of the mesoscale convective vortex of 10–13 June 2003," *Monthly Weather Review*, **135**(4), pp. 1544–1563.
- [21] ZHANG, F. and J. SIPPEL (2009) "Effects of Moist Convection on Hurricane Predictability," *Journal of the Atmospheric Sciences*, **66**(7), pp. 1944–1961.
- [22] HONG, S., J. DUDHIA, and S. CHEN (2004) "A revised approach to ice microphysical processes for the bulk parameterization of clouds and precipitation," *Monthly Weather Review*, **132**(1), pp. 103–120.
- [23] NOH, Y., W. CHEON, S. HONG, and S. RAASCH (2003) "Improvement of the K-profile model for the planetary boundary layer based on large eddy simulation data," *Boundary-Layer Meteorology*, **107**(2), pp. 401–427.
- [24] GRELL, G. and D. DEVENYI (2002) "A generalized approach to parameterizing convection combining ensemble and data assimilation techniques," *Geophysical Research Letters*, **29**(14), pp. 38–1.
- [25] ZHANG, F., N. BEI, R. ROTUNNO, C. SNYDER, and C. EPIFANIO (2007) "Mesoscale predictability of moist baroclinic waves: Convection-permitting experiments and multistage error growth dynamics," *Journal of the Atmospheric Sciences*, **64**(10), pp. 3579–3594.
- [26] BARKER, D., W. HUANG, Y. GUO, A. BOURGEOIS, and Q. XIAO (2004) "A three-dimensional variational data assimilation system for MM5: Implementation and initial results," *Monthly Weather Review*, **132**(4).
- [27] SIPPEL, J. and F. ZHANG (2008) "A Probabilistic Analysis of the Dynamics and Predictability of Tropical Cyclogenesis," *Journal of the Atmospheric Sciences*, **65**(11), pp. 3440–3459.